
















RESEARCH ARTICLE

10.1029/2023AV000875

Decadal Trends in the Oceanic Storage of Anthropogenic Carbon From 1994 to 2014

Peer Review The peer review history for this article is available as a PDF in the Supporting Information.

Jens Daniel Müller¹ , N. Gruber¹ , B. Carter^{2,3} , R. Feely³ , M. Ishii⁴ , N. Lange⁵ , S. K. Lauvset⁶ , A. Murata⁷ , A. Olsen⁸ , F. F. Pérez^{9,10} , C. Sabine¹¹ , T. Tanhua⁵ , R. Wanninkhof¹² , and D. Zhu¹ 

Key Points:

- The global ocean storage of anthropogenic carbon grew by 29 ± 3 and 27 ± 3 Pg C dec⁻¹ from 1994 to 2004 and 2004 to 2014, respectively
- The change in oceanic storage of anthropogenic carbon relative to the atmospheric CO₂ growth decreased by $15 \pm 11\%$ from the first to the second decade
- This reduction is attributed to a decrease of the ocean buffer capacity and changes in ocean circulation

¹Environmental Physics, Institute of Biogeochemistry and Pollutant Dynamics, ETH Zurich, Zurich, Switzerland,

²Cooperative Institute for Climate, Ocean, and Ecosystem Studies, University of Washington, Seattle, WA, USA, ³Pacific Marine Environmental Laboratory, National Oceanic and Atmospheric Administration, Seattle, WA, USA, ⁴Meteorological Research Institute, Japan Meteorological Agency, Tsukuba, Japan, ⁵GEOMAR Helmholtz Centre for Ocean Research Kiel, Kiel, Germany, ⁶NORCE Norwegian Research Centre, Bjerknes Centre for Climate Research, Bergen, Norway, ⁷Japan Agency for Marine–Earth Science and Technology, Yokosuka, Japan, ⁸Geophysical Institute, University of Bergen and Bjerknes Centre for Climate Research, Bergen, Norway, ⁹Instituto de Investigaciones Marinas (IIM), CSIC, Vigo, Spain, ¹⁰Oceans Department, Stanford University, Stanford, CA, USA, ¹¹University of Hawaii at Manoa, Honolulu, HI, USA, ¹²Atlantic Oceanographic and Meteorological Laboratory, National Oceanographic and Atmospheric Administration, Miami, FL, USA

Supporting Information:

Supporting Information may be found in the online version of this article.

Correspondence to:

J. D. Müller,
jensdaniel.mueller@usys.ethz.ch

Citation:

Müller, J. D., Gruber, N., Carter, B., Feely, R., Ishii, M., Lange, N., et al. (2023). Decadal trends in the oceanic storage of anthropogenic carbon from 1994 to 2014. *AGU Advances*, 4, e2023AV000875. <https://doi.org/10.1029/2023AV000875>

Received 17 JAN 2023
Accepted 19 MAY 2023
Corrected 30 AUG 2023

This article was corrected on 30 AUG 2023. See the end of the full text for details.

Author Contributions:

Conceptualization: Jens Daniel Müller, N. Gruber
Data curation: Jens Daniel Müller, N. Lange
Formal analysis: Jens Daniel Müller
Funding acquisition: N. Gruber

Abstract The oceanic uptake and resulting storage of the anthropogenic CO₂ (C_{ant}) that humans have emitted into the atmosphere moderates climate change. Yet our knowledge about how this uptake and storage has progressed in time remained limited. Here, we determine decadal trends in the storage of C_{ant} by applying the eMLR(C*) regression method to ocean interior observations collected repeatedly since the 1990s. We find that the global ocean storage of C_{ant} grew from 1994 to 2004 by 29 ± 3 Pg C dec⁻¹ and from 2004 to 2014 by 27 ± 3 Pg C dec⁻¹ ($\pm 1\sigma$). The storage change in the second decade is about $15 \pm 11\%$ lower than one would expect from the first decade and assuming proportional increase with atmospheric CO₂. We attribute this reduction in sensitivity to a decrease of the ocean buffer capacity and changes in ocean circulation. In the Atlantic Ocean, the maximum storage rate shifted from the Northern to the Southern Hemisphere, plausibly caused by a weaker formation rate of North Atlantic Deep Waters and an intensified ventilation of mode and intermediate waters in the Southern Hemisphere. Our estimates of the C_{ant} accumulation differ from cumulative net air-sea flux estimates by several Pg C dec⁻¹, suggesting a substantial and variable, but uncertain net loss of natural carbon from the ocean. Our findings indicate a considerable vulnerability of the ocean carbon sink to climate variability and change.

Plain Language Summary The ocean takes up about 30% of the anthropogenic CO₂ that is emitted to the atmosphere by human activities. The removal of this anthropogenic CO₂ from the atmosphere counteracts climate change. The rate at which the ocean takes up anthropogenic CO₂ is controlled by its transport from the surface to the depth of the ocean, where most of it accumulates. Thus, we can quantify and understand the oceanic uptake by keeping track of the accumulation of anthropogenic CO₂ in the ocean interior. In this study, we use a global collection of measurements of CO₂ in seawater to infer the temporal evolution of this accumulation between 1994 and 2014. We find that the ocean continued to act as a strong sink for CO₂ over this period, removing, on average, nearly 30 billion tons of carbon per decade. However, we also detect a possible weakening of this uptake, since the accumulation of anthropogenic CO₂ during the second decade was not as large as expected from the increase in atmospheric CO₂. Our findings suggest that the ocean sink for CO₂ might further shrink as climate change progresses.

1. Introduction

As a consequence of climate change, the ocean is warming, acidifying, becoming more stratified, and experiencing increasing winds and an intensified hydrological cycle (Cheng et al., 2022; IPCC, 2019; Jiang et al., 2019; Li et al., 2020; Young & Ribal, 2019). While the ocean itself has been vital to mitigate climate change over the past two centuries through its removal of CO₂ from the atmosphere (DeVries, 2014; Gruber et al., 2023; Khatiwala et al., 2009), a key concern is whether the ocean carbon sink will maintain its function in a changing climate. Models and observation-based estimates agree that since the beginning of the industrial period, the ocean has

© 2023. The Authors.

This is an open access article under the terms of the [Creative Commons Attribution License](https://creativecommons.org/licenses/by/4.0/), which permits use, distribution and reproduction in any medium, provided the original work is properly cited.

Investigation: Jens Daniel Müller
Methodology: Jens Daniel Müller, N. Gruber, D. Zhu
Software: Jens Daniel Müller
Supervision: Jens Daniel Müller, N. Gruber
Validation: Jens Daniel Müller, N. Gruber, D. Zhu
Visualization: Jens Daniel Müller
Writing – original draft: Jens Daniel Müller
Writing – review & editing: Jens Daniel Müller, N. Gruber, B. Carter, R. Feely, M. Ishii, N. Lange, S. K. Lauvset, A. Murata, A. Olsen, F. F. Pérez, C. Sabine, T. Tanhua, R. Wanninkhof, D. Zhu

taken up roughly 30% of the total human CO₂ emissions due to fossil fuel combustion, cement production, and land use change (Crisp et al., 2022; Friedlingstein et al., 2022; Gruber et al., 2019; Khatiwala et al., 2009, 2013; Sabine et al., 2004). The observations from the first global survey of CO₂ in the ocean interior during the 1980s and 1990s (Key et al., 2004; Wallace, 1995) provided an important pillar for this consensus, demonstrating that between ~1800 and 1994, the ocean had taken up 118 ± 19 Pg (10^{15} g) of anthropogenic carbon from the atmosphere (Sabine et al., 2004). Anthropogenic carbon (C_{ant}) refers to the additional carbon present in the ocean-atmosphere-land system due to human CO₂ emissions to the atmosphere (Gruber et al., 2023). We denote temporal changes in the ocean interior content of C_{ant} as ΔC_{ant} .

Another pillar supporting the consensus about the strength of the oceanic C_{ant} sink was established when the observational data were extended with the ocean interior measurements gathered during the second cycle of the repeat hydrography program in the framework of GO-SHIP, the Global Ocean Ship-based Hydrographic Investigations Program (Talley et al., 2016). Applying a modified version of the extended Multiple Linear Regression method (eMLR(C*)) to the data available until the early 2010s, Gruber et al. (2019) demonstrated that the ocean took up an additional 34 ± 4 Pg C of C_{ant} from 1994 to 2007 corresponding to a mean decadal storage rate of 26 ± 3 Pg C dec⁻¹. This globally integrated storage rate is indistinguishable from the growth that one would predict from the total C_{ant} storage in 1994 and assuming an increase of this inventory proportional with the rise in atmospheric CO₂. Hence, this finding suggested that up to 2007, the globally integrated oceanic C_{ant} sink had been responding in near steady-state fashion to the anthropogenic perturbation, without showing any discernible impact of climate change.

However, a first indication of a deviation from this proportional steady-state accumulation emerged in the spatial patterns of the reconstructed changes in C_{ant} storage between 1994 and 2007 (Gruber et al., 2019). By comparing these changes with those expected on the basis of the reconstructed storage of C_{ant} for 1994 (Sabine et al., 2004), Gruber et al. (2019) found a roughly 20% decrease of the storage rate in the North Atlantic compensated by an increased storage rate in the South Atlantic. However, the robustness of these shifts remains unclear, because they were derived from the comparison of results from two different methodological approaches, both with poorly characterized uncertainties at the regional scale.

A second indication of a deviation from the proportional steady-state uptake emerged from the analysis of the difference between the ocean interior storage changes of C_{ant} and the net air-sea fluxes of CO₂ determined based on sea surface observations of pCO₂ (Landschützer et al., 2016). These surface flux estimates include the transfer of both anthropogenic CO₂ and natural CO₂ across the air-sea interface, with the latter referring to the carbon that was already present in the Earth System in preindustrial times (Gruber et al., 2023). The difference between storage and net fluxes amounted to 5 ± 3 Pg C over the 1994–2007 period and was interpreted as a non-steady state (i.e., climate-driven) outgassing of natural CO₂ from the ocean.

While some studies suggested that the outgassing of natural CO₂ may contribute to a long-term saturation of the oceanic carbon sink (Le Quéré et al., 2007), recent surface flux estimates actually indicate that the net global ocean carbon sink increased strongly over the past decade (Fay et al., 2021; Friedlingstein et al., 2022). But for reasons not yet fully understood, Global Ocean Biogeochemical Models (GOBMs) tend to suggest a smaller increase in uptake since around 2002 compared to the estimates based on the surface ocean pCO₂ observations (Friedlingstein et al., 2022; Hauck et al., 2020). Hence, the discrepancy between these two methods increased over the 2010s, culminating in the surface flux products estimating a 0.6 Pg C yr⁻¹ stronger sink than the GOBMs for the 2010s (Friedlingstein et al., 2022). This discrepancy forces the authors of the Global Carbon Budget (GCB) to assign only a medium confidence level to the ocean sink estimate, as it represents the mean of the GOBMs and the surface flux products (Friedlingstein et al., 2022). Thus, independent information about the oceanic uptake of CO₂ by extending the knowledge about the oceanic accumulation of C_{ant} beyond 2007 would be very useful to help resolving this discrepancy and to better understand the drivers for the changes in the strength of the ocean carbon sink.

Some independent information about the evolution of the ocean sink beyond 2007 is already available from regional analyses of the accumulation of C_{ant} over the last few decades. In the Pacific Ocean the C_{ant} inventory change was found to have increased from 8.8 ± 1.1 Pg C dec⁻¹ between 1995 and 2005 to 11.7 ± 1.1 Pg C dec⁻¹ between 2005 and 2015 (Carter et al., 2019). Even more pronounced increases were reported for the North Atlantic Ocean with an intensification of the C_{ant} storage from 1.9 ± 0.4 Pg C dec⁻¹ for the 1993–2003

period to 4.4 ± 0.9 Pg C dec⁻¹ from 2003 to 2014 (Wanninkhof et al., 2010; Woosley et al., 2016). While Woosley et al. (2016) reported a rather steady uptake behavior in the South Atlantic, Gao et al. (2022) found that the rates of C_{ant} storage accelerated from the 1990s to the 2000s. In all regional studies, the temporal variability of the C_{ant} storage was attributed to changing ventilation patterns of the upper ocean. However, differences in time periods and statistical methods applied in the regional studies limit their synoptic assessment and prevent combining them into a global reconstruction of the oceanic increase in C_{ant} storage since 2007.

Such an extension of the reconstruction of the global increase in C_{ant} storage beyond 2007 is the key aim of this study. Our work profits from including $\sim 100,000$ additional observations of dissolved inorganic carbon (DIC) and related biogeochemical variables collected over the 2010s, which were compiled, quality-controlled, and made available by GLODAP, the Global Ocean Data Analysis Project (Lauvset et al., 2021). By consistently determining the storage increase between 1994 and 2004, and between 2004 and 2014, and benefitting from the reconstructed storage of C_{ant} for 1994, we can investigate for the first time the temporal evolution of the global increase in the oceanic storage of C_{ant} . This permits us to address whether the ocean has maintained its vital sink function in a changing climate. Our global-scale reconstruction of the oceanic storage of C_{ant} further serves as an important independent reference point for the ocean carbon sink estimates established by other means, especially in the context of the GCB (Friedlingstein et al., 2022) and the Intergovernmental Panel on Climate Change (IPCC) (Canadell et al., 2021).

2. Material and Methods

2.1. Overview of the Approach

Our global-scale analysis of the changes in the content of C_{ant} (ΔC_{ant}) is based on measurements of the dissolved inorganic carbon (DIC) content and related hydrographical and biogeochemical properties gathered from 1989 to 2020 and synthesized in the data product GLODAPv2.2021 (Lauvset et al., 2021; Olsen et al., 2016). This data product includes high-quality measurements from reoccupied sections for the purposes of diagnosing long term climate signals such as the accumulation of C_{ant} . The majority of the data used in this study stem from the JGOFS/WOCE global CO₂ survey conducted in the 1980s and 1990s (Key et al., 2004; Wallace, 1995), the repeat hydrography program GO-SHIP that began in 2003 and is now completing its second cycle (Sloyan et al., 2019; Talley et al., 2016), as well as a number of additional programs, including INDIGO, SAVE, TTO, JOIS, and GEOSECS (Key et al., 2004, and references therein). In addition to DIC, our analysis requires observations of salinity (S), temperature (T), total alkalinity (TA), oxygen (O₂), the apparent oxygen utilisation (AOU), silicate (Si(OH)₄), nitrate (NO₃⁻), and phosphate (PO₄³⁻). To extract the ΔC_{ant} signal from these data, we use the eMLR(C*) method (Clement & Gruber, 2018; Gruber et al., 2019) with a few modifications (see details below and in Text S2 in Supporting Information S1).

Our application of the eMLR(C*) method employs the following steps:

1. The semi-conservative tracer C* (Gruber et al., 1996; Gruber & Sarmiento, 2002) is calculated from DIC as $C^* = \text{DIC} - 117 \times \text{PO}_4^{3-} - 0.5 \times (\text{TA} + 16 \times \text{PO}_4^{3-})$. This conversion from DIC to C* removes a substantial part of the inorganic carbon variability that is due to ocean interior redistributions and biogeochemical transformations of natural carbon.
2. The observations are clustered in neutral density slabs (Text S2.1 in Supporting Information S1) and ocean regions (Figure S1 in Supporting Information S1), and assigned to one of the three sampling periods 1989–1999, 2000–2009, or 2010–2020 (Figure 1).
3. Within each sampling period, the observed C* is adjusted to the respective reference year (t_{ref}) 1994, 2004, or 2014 assuming a transient steady state increase of C_{ant} (Gammon et al., 1982).
4. Within each neutral density slab and ocean region, a set of multiple linear regression (MLR) models are fitted with $C^*(t_{\text{ref}})$ as target variable and all possible combinations of at least 2 out of the 7 considered predictor variables S, T, O₂, AOU, Si(OH)₄, NO₃⁻, PO₄³⁻.
5. The 10 best common MLR models for two compared sampling periods are selected within each density slab and ocean region based on the summed root mean squared error (RMSE), after excluding MLRs with strong multicollinearity between the predictors (Text S2.2 in Supporting Information S1).

6. The decadal change in anthropogenic carbon is computed as the difference between the average C^* distribution for each sampling period, that is, $\Delta C_{\text{ant}} = C^*(t_{\text{ref},n+1}) - C^*(t_{\text{ref},n})$, where the C^* distributions are predicted (“mapped”) for each t_{ref} by applying the selected MLRs to a common set of predictor climatologies.
7. In surface waters, ΔC_{ant} is predicted based on a transient equilibrium approach (McNeil et al., 2003), which assumes that the increase of the surface ocean $p\text{CO}_2$ follows that of the atmosphere closely. This approach aims to avoid biases introduced by the seasonal and interannual variability of C^* and the predictor variables.

The most important differences we introduced relative to the methods described by Clement and Gruber (2018) and Gruber et al. (2019) are detailed in Section 2.3 and include a more thorough selection of the predictor variables and MLR models, a more robust and standardised quantification of uncertainties, and an assessment of structural reconstruction uncertainties through tests with synthetic data, which were performed in parallel to the analysis of the real-world observations. Our reconstruction of ΔC_{ant} with the eMLR(C^*) method involves a number of choices regarding the configuration of the method. In Sections 2.2 and 2.3 we describe the standard configuration that we use to derive the results we report as our best informed estimates. In Section 2.4, we describe a number of reasonable alternative configurations. We use the offsets between results obtained with these plausible alternatives and the standard configuration as a basis for determining the uncertainty.

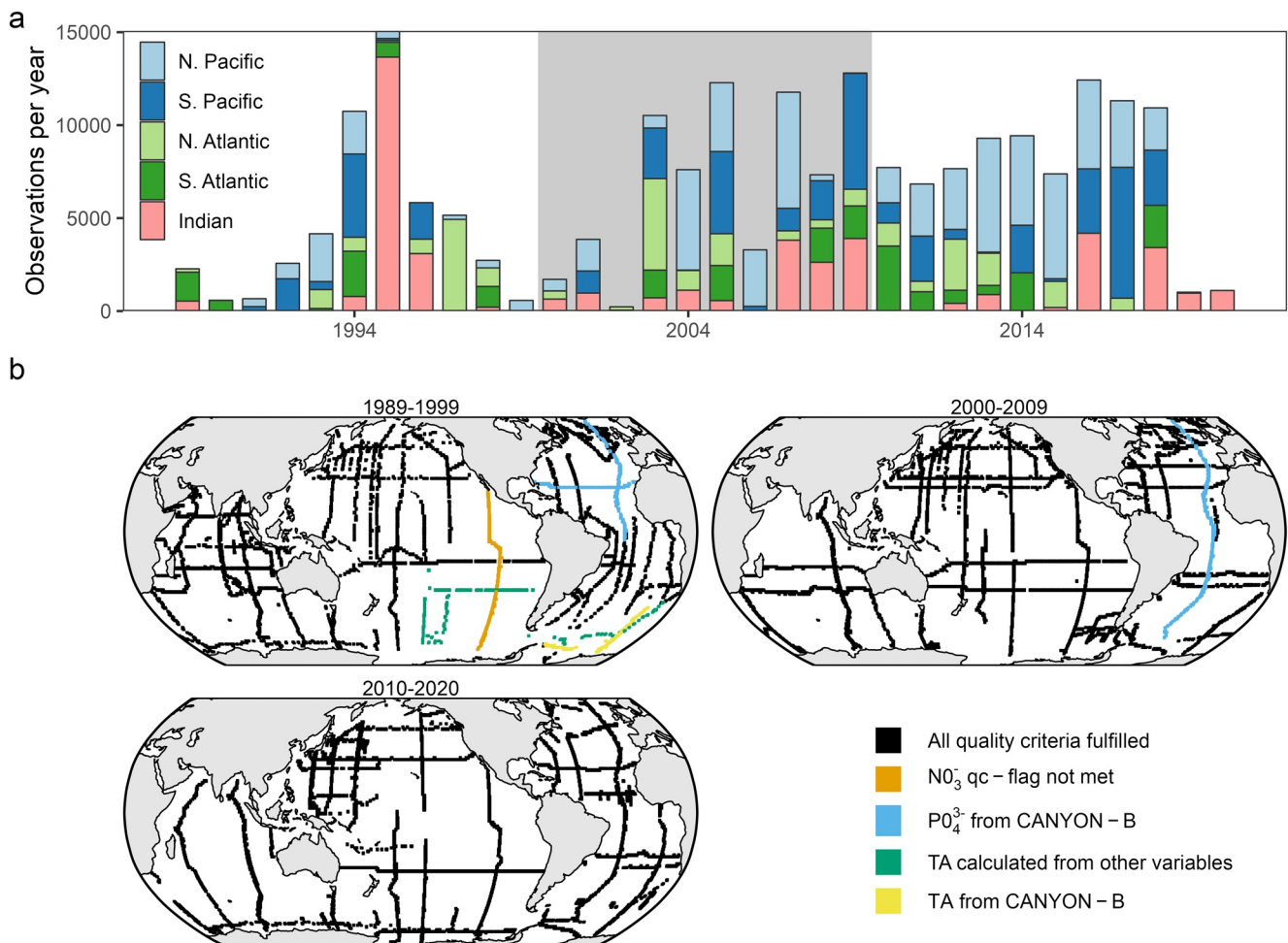


Figure 1. Spatio-temporal coverage of observations from 1989 to 2020 as provided through GLODAPv2.2021 and after applying our flagging criteria. (a) Number of observations per year, where colors distinguish sampling regions according to the basin mask definition “5” in Figure S1 in Supporting Information S1. The shaded background indicates the assigned sampling periods 1989–1999 ($t_{\text{ref},1} = 1994$), 2000–2009 ($t_{\text{ref},2} = 2004$), and 2010–2020 ($t_{\text{ref},3} = 2014$). (b) Map of observations as used in our standard case for the three sampling periods. Cruises that fulfilled all flagging criteria are displayed in black, while cruises for which one parameter did not fulfill all criteria but were still included (see also Table S1 in Supporting Information S1) are highlighted in color.

2.2. Data

This study relies on ocean interior observations of DIC, TA, S, T, O₂, Si(OH)₄, NO₃⁻, and PO₄³⁻ collected in the global ocean from 1989 through 2020 (Figure 1) and provided through GLODAPv2.2021 (Lauvset et al., 2021; Olsen et al., 2016). The apparent oxygen utilisation was calculated from oxygen, salinity, and conservative temperature (Graham & McDougall, 2013) according to the solubility from Weiss (1970) and used as an additional predictor variable. Observations were filtered based on the GLODAP flagging scheme, using only highest-quality data identified as those with a f-flag value of 2, which indicates acceptable, measured data according to a simplified version of the WOCE flagging scheme, and a qc-flag value of 1, which indicates adjusted or unadjusted data that have undergone GLODAP's full secondary quality control. With a few exceptions, only samples were included for which all required variables fulfill the strictest quality criteria. We deviated from this only for cases where our tests of the eMLR(C*) method with synthetic data (see Text S5 in Supporting Information S1) revealed that omitting observations because of only one missing variable increased the biases of the ΔC_{ant} reconstructions. In these cases either data that did not fulfill the strictest quality criteria were included (7,609 samples, 3.7% of all samples), or missing data were filled (7,305 samples, 3.5%) using CANYON-B (Bittig et al., 2018) predictions (see Text S1.3 in Supporting Information S1). In total, we used 206,836 samples for our standard case reconstruction.

Although the GLODAP data have already undergone a secondary quality control and are—if required—adjusted to improve their internal consistency, we applied a number of additional adjustments to the DIC, TA, and phosphate observations. These data adjustments are supported by multiple independent lines of evidence and quantified based either on our decade-by-decade reanalysis of deep water crossovers originally determined by GLODAP, or on previously unaccounted offsets in the measurements of certified reference materials (CRM) for DIC and TA (see Text S1.2 in Supporting Information S1 for details; Johnson et al., 1998, 2002; Millero et al., 1998). This affected the majority of the DIC and TA measurements from the Indian Ocean in the 1990s (12,843 samples, 6.2% of all samples), and the DIC, TA, and phosphate measurements in the North Pacific from the 2010s (35,395 samples, 17.2% of all samples). Our proposed adjustments of the Indian Ocean data were formally accepted by GLODAP and applied in the release of GLODAPv2.2022 (Lauvset et al., 2022). In contrast, the proposed adjustments for the North Pacific are still under discussion by the GLODAP community, and while well justified and likely attributable to measurement inconsistencies (Fong & Dickson, 2019; Olsen et al., 2019; Sharp & Byrne, 2020), currently need to be viewed as preliminary. We thus discuss the relevance of the North Pacific adjustments for our results and conclusions in detail. The magnitude of these additional adjustments are generally small (<2 $\mu\text{mol kg}^{-1}$ for DIC, <4 $\mu\text{mol kg}^{-1}$ for TA, and <1% for PO₄³⁻) and below the adjustment limits normally considered by GLODAP. Still, these adjustments proved to be critical in our work, since an offset of 1 $\mu\text{mol kg}^{-1}$ in DIC integrated over 3,000 m amounts to a column inventory offset of $\sim 3 \text{ mol m}^{-2}$, which is of similar magnitude as some of the decadal changes we are aiming to detect.

For the purpose of predicting the C* distributions, we used the objectively analyzed climatology for the 1981–2010 period for salinity and temperature from the World Ocean Atlas 2018 (Locarnini et al., 2019; Zweng et al., 2019), in combination with O₂, Si(OH)₄, NO₃⁻, and PO₄³⁻ from the global interior ocean mapped climatology based on GLODAPv2 (Lauvset et al., 2016). The climatological distribution of AOU was calculated in accordance with the observational data. For atmospheric CO₂ (CO_{2,atm}) data we use the globally averaged marine surface annual mean data provided by NOAA/GML (Lan et al., 2022).

2.3. Standard Configuration of the eMLR(C*) Method

In the following, we describe the main changes of the eMLR(C*) method in comparison to the previous analysis by Gruber et al. (2019). Further minor configuration changes are presented in Text S2 in Supporting Information S1.

2.3.1. Temporal Clustering and C* Adjustment to Reference Year

For the temporal clustering of the data, we assigned each observation to one of the following three sampling periods (start and end years included):

$$1989\text{--}1999 (t_{\text{ref},1} = 1994)$$

$$2000\text{--}2009 (t_{\text{ref},2} = 2004)$$

$$2010\text{--}2020 (t_{\text{ref},3} = 2014)$$

with the assigned reference years (t_{ref}) given in parenthesis.

Based on these three sampling periods, we estimated the C_{ant} storage changes between the reference years 1994–2004 and 2004–2014 (Figure 1). The ΔC_{ant} estimates represent the changes over exactly 10 years, from mid-year of the first to mid-year of the second reference year. In addition, we determined ΔC_{ant} directly for the 20 years period 1994–2014.

The adjustment of C^* from the time of sample collection (t) to the reference year (t_{ref}) was calculated as $C^*(t_{\text{ref}}) = C^*(t) - \delta(t) * C_{\text{ant}}(t_{\text{ref}})$, with $\delta(t) = \Delta \text{CO}_{2,\text{atm}}(t - t_{\text{ref}}) / \Delta \text{CO}_{2,\text{atm}}(t_{\text{ref}} - t_{\text{pi}})$, where t_{pi} indicates preindustrial times (~ 1800) and $\Delta \text{CO}_{2,\text{atm}}$ is the change in atmospheric CO_2 . We estimated the C_{ant} content in the reference year ($C_{\text{ant}}(t_{\text{ref}})$), by adding a proportional fraction of the reconstructed increase in C_{ant} over 13 years between 1994 and 2007 ($\Delta C_{\text{ant}}(1994\text{--}2007)$, Gruber et al., 2019) to the reconstructed C_{ant} in 1994 ($C_{\text{ant}}(1994)$, Sabine et al., 2004), that is, $\Delta C_{\text{ant}}(1994\text{--}t_{\text{ref}}) = (t_{\text{ref}} - 1994) * \Delta C_{\text{ant}}(1994\text{--}2007) / 13$ years.

2.3.2. Spatial Clustering and Subsetting

For the fitting of the MLR models and mapping of ΔC_{ant} in the standard configuration, we clustered the observations and predictor climatologies horizontally into the Atlantic, Pacific and Indian Ocean, according to mask “3” of our basin mask definitions (Figure S1 in Supporting Information S1) derived from the World Ocean Atlas (Garcia et al., 2019). To assess the contribution of the impact of this choice on the uncertainty of the reconstructed changes in C_{ant} , we investigated five other basin configurations (Figure S1 in Supporting Information S1). For clustering in the vertical dimension, we used the same neutral density (Jackett & McDougall, 1997) levels as employed by Gruber et al. (2019). Surface water samples collected shallower than 100 m were excluded from the MLR fitting to avoid seasonally biased observations.

2.3.3. Mapping C^* and ΔC_{ant}

The spatial distribution of C^* was mapped by predicting the best MLR models of each reference year with climatological distributions of the predictor variables. For this purpose, the 10 best MLR models within each spatial cluster were selected as those with the lowest summed RMSE for the two paired sampling periods following Clement and Gruber (2018). The 10 individually mapped C^* distributions were then averaged and subtracted to derive the mean ΔC_{ant} distribution. In contrast to prior applications of the method, we included negative mapped ΔC_{ant} values, since (a) ΔC_{ant} can regionally be negative when water with low C_{ant} displaces water with high C_{ant} , (b) setting negative values to zero could lead to positively biased ΔC_{ant} inventories, and (c) our tests with synthetic data revealed a tendency to lower biases when negative values were retained.

2.3.4. Surface Equilibrium ΔC_{ant}

In the standard configuration, the equilibrium ΔC_{ant} distribution at the sea surface was computed based on a rearranged definition of the Revelle factor, γ , as $\Delta C_{\text{ant,eq}}(t_{\text{ref},n} - t_{\text{ref},n+1}) = 1/\gamma \times \text{DIC}/\text{pCO}_2 \times \Delta \text{CO}_{2,\text{atm}}(t_{\text{ref},n+1} - t_{\text{ref},n})$, where DIC, pCO_2 and γ are the climatological surface values (Lauvset et al., 2016) adjusted to the mean $\text{CO}_{2,\text{atm}}$ of each analysis period. This adjustment of the climatological surface CO_2 -system parameters to the mean $\text{CO}_{2,\text{atm}}$ was achieved by calculating as a first step the surface pCO_2 in 2002 based on the climatological values for temperature, salinity, DIC and TA, which are normalized to the same year (Lauvset et al., 2016). In a second step, the surface ocean pCO_2 was shifted according to the change in $\text{CO}_{2,\text{atm}}$, and DIC and γ were recalculated based on the new surface pCO_2 . Thus, our surface equilibrium approach takes changes in the surface ocean buffer capacity into consideration. All CO_2 -system calculations were done with the R-package seacarb (Gattuso et al., 2021) using the CO_2 dissociation constants from Lueker et al. (2000), the fluoride association constant from Perez and Fraga (1987) or Dickson and Riley (1979) at temperatures below 9°C and the acidity constant of hydrogen sulphide from Dickson (1990). To assess the uncertainties associated with this equilibrium ΔC_{ant} estimate, we also used OceanSODA, an independent observation-based estimate of the increase in surface DIC (Gregor & Gruber, 2021).

While previous studies defined a distinct depth and neutral density threshold to separate water masses for which the surface equilibrium or eMLR(C^*) reconstructions are used to determine ΔC_{ant} , we blend both estimates smoothly over the top 200 m. For this purpose, the equilibrium ΔC_{ant} is calculated at the sea surface only, while the eMLR-based ΔC_{ant} is initially mapped across the entire water column. In a post processing step, the surface- and eMLR-based ΔC_{ant} estimates are averaged proportionally according to the water depth across the upper 200 m (e.g., 75% surface-based and 25% eMLR(C^*)-based estimate at 50 m water depth).

2.4. Computation of Global ΔC_{ant} Inventories and Sensitivities

Column inventories and inventories of ΔC_{ant} in this study represent integrals across the upper 3,000 m of the water column. ΔC_{ant} reconstructions below 3,000 m are not included in integrals to avoid the imprint of ΔC_{ant} uncertainties

that are small in terms of amount content but considerable in terms of integrated inventory changes. Instead, we follow previous studies and account for C_{ant} storage changes below 3,000 m by adding 2% to our global ΔC_{ant} inventories. This deep ocean scaling represents the fraction of the total C_{ant} inventory in 1994 beneath 3,000 m according to Sabine et al. (2004). We further scale our global inventories for the storage of C_{ant} in unmapped regions according to previously determined fractions of the global C_{ant} storage that occurs in these regions, namely 2% in the Arctic Ocean (Tanhua et al., 2009), 1.5% in the Mediterranean Sea (Palmiéri et al., 2015), 1% in the Nordic Seas (Olsen et al., 2010), and 0.3% in the Sea of Japan (Park et al., 2006). In sum, the upscaling amounts to 7% of our directly mapped global ΔC_{ant} inventory. Regional inventories refer to the integral of directly mapped ΔC_{ant} distributions and no areal scaling was applied, for example, the regional inventory of the Atlantic Ocean does not account for storage in the Mediterranean Sea. Thus, our global inventory differs from the sum of the regional inventories by 7%.

To relate the global decadal change in the oceanic C_{ant} inventory ($\text{Inv}(\Delta C_{\text{ant}})$) to the primary driver of the C_{ant} uptake, that is, the increase in atmospheric CO_2 over the same decade ($\Delta \text{CO}_{2,\text{atm}}$), we compute the storage sensitivity $\beta = \text{Inv}(\Delta C_{\text{ant}})/\Delta \text{CO}_{2,\text{atm}}$. Globally, the sensitivity β measures how much additional anthropogenic carbon the ocean takes up and stores (Gruber et al., 2023; Ríos et al., 2012) in response to the increase in atmospheric CO_2 . As long as atmospheric CO_2 increases close to exponentially, as was the case for the past 50 years, the sensitivity β is expected to remain constant, provided that ocean circulation remains in steady-state (Keeling, 1979) and ocean chemistry does not change. This implies that under these circumstances, changes in the oceanic storage of C_{ant} scale linearly with changes in atmospheric CO_2 , that is, $\text{Inv}(\Delta C_{\text{ant}}) = \beta * \Delta \text{CO}_{2,\text{atm}}$ (Gruber et al., 2023). Conversely, deviations from this linear scaling indicate changes in ocean circulation or other changes affecting β , such as the reduction in the oceanic buffering capacity owing to ongoing ocean acidification. Note, however, that this metric will be less useful when the atmospheric CO_2 growth rates will start to fall (see Gruber et al. (2023) for discussion).

For our regional and basin-scale analyses, we will use the regional expression of this sensitivity, that is, the area-normalized storage sensitivity β_{area} , to achieve direct comparability of the storage sensitivity across different regions. It is defined as $\beta_{\text{area}} = \beta/A$, where A is the surface area of the region under consideration.

2.5. Determination of Uncertainty and Method Testing

The most important sources of uncertainty associated with the eMLR(C^*) method are structural in nature and involve choices associated with the configuration of the method (Clement & Gruber, 2018; Gruber et al., 2019). We identified the following six configuration choices as critical (a) the regional clustering of the data, (b) the approach to perform data adjustments, (c) the nutrient used to compute the target variable C^* , (d) the approach to estimate surface ocean ΔC_{ant} , (e) the gap-filling of flagged data, and (f) the choice of predictor climatologies. In addition, we consider (g) an uncertainty contribution in our global ΔC_{ant} inventories arising from the scaling to account for C_{ant} storage changes in unmapped waters.

To assess the impact of these choices and to obtain an estimate of uncertainty of our reconstructions, we have reconstructed a set of total 10 alternative estimates of ΔC_{ant} using modified choices for each of the six configurations listed above. These modifications of the eMLR(C^*) configuration are described in detail in Text S4 in Supporting Information S1. We base our estimate of uncertainty on the ΔC_{ant} offsets between the standard case and the reconstructions obtained with the configuration changes. The individual offsets are considered as independent uncertainty contributions and combined as the square root of the sum of the squares (RSS) to derive the standard uncertainty ($\pm 1\sigma$) of our reconstructions, which we consider as a 68% confidence interval. Throughout the results and discussion, we report all results together with this $\pm 1\sigma$ uncertainty. In figures, we display also the expanded $\pm 2\sigma$ uncertainty representing a confidence interval of 95%. For each variable that is derived from a primary ΔC_{ant} estimate (e.g., the decadal difference between two ΔC_{ant} estimates, the ocean-borne fraction, etc.) we combine individual uncertainties through standard error propagation.

In order to independently assess the quality of our ΔC_{ant} reconstructions against a known truth, we used synthetic data generated from the GOBM CESM-ETHZ (Doney et al., 2009; Hauck et al., 2020; Yang et al., 2017) following the approach of Clement and Gruber (2018). The GOBM is a hindcast model forced with reanalyzed atmospheric data (Tsujino et al., 2018) and the observed atmospheric CO_2 trajectory. The synthetic data set was generated by subsetting the model output in space and time according to availability of real-world observations. The eMLR(C^*) approach was then applied to the synthetic data set to reconstruct ΔC_{ant} . The comparison of the reconstructed ΔC_{ant} to the known model truth allows us to determine the biases of the reconstruction. Details and results of this assessment are given in the Text S5 in Supporting Information S1.

In order to assess the sensitivity of our reconstructions to other sources of uncertainty, such as the limited sampling of the spatio-temporal variability of the changes in DIC, we performed additional eMLR(C*) analyses, wherein we pushed the configurations beyond the limits of what we consider a reasonable modification. For example, we limited the observations to those from repeatedly occupied sections, used other DIC variants than C* as target variable and omitted the data adjustments (see Section 4.2). In contrast, other choices associated with the application of the eMLR(C*) method have shown to be of minor relevance for the uncertainty of the reconstructed ΔC_{ant} and were thus not considered in the uncertainty assessment (Text S2 in Supporting Information S1). This applies, for example, to the choice of the a priori C_{ant} estimate used for the adjustment of C* to the reference year (Clement & Gruber, 2018).

3. Results

3.1. Column Inventories

The storage changes in anthropogenic carbon (ΔC_{ant}) integrated over the upper 3,000 m (referred to as column inventories) reveal strong similarities during both decades of our analysis, that is, between 1994 and 2004, and between 2004 and 2014 (Figures 2a and 2b). The ΔC_{ant} column inventories vary markedly with latitude. The highest mean decadal C_{ant} storage changes of about $10 \text{ mol m}^{-2} \text{ dec}^{-1}$ located near the center of the subtropical gyres (30–40°N/S) are about twice as high as those in the equatorial regions (10°N/S) and in the Southern Ocean south of 60°S. In the Southern Hemisphere, the consistently high ΔC_{ant} column inventories in all subtropical gyres form a circumpolar band, while in the Northern Hemisphere the storage changes per unit area in the Atlantic exceed those in the Pacific roughly by a factor of two. The general patterns of our ΔC_{ant} reconstructions are reminiscent of those reconstructed for the pre-industrial to 1994 period (Sabine et al., 2004) and for the 1994 to 2007 period (Gruber et al., 2019), supporting in first approximation the expectation of a steady-state increase in the oceanic storage of C_{ant} . We also note that our ΔC_{ant} column inventory reconstructions for the 1994–2007 period (Figure S6 in Supporting Information S1) confirm those reported by Gruber et al. (2019) for the same period, supporting the consistency of our approaches and estimates despite the modifications of the eMLR(C*) method and our use of an updated database.

While the general pattern of the increases in the C_{ant} column inventories are similar in the two decades, there are distinct differences (Figure 2c). These decadal differences are most pronounced in the Atlantic Ocean, where we find a shift of the highest ΔC_{ant} column inventories from the Northern to the Southern Hemisphere. In the subtropical latitudes (20–50°N) of the North Atlantic, the mean, area-weighted ΔC_{ant} column inventory in the second decade is $3.7 \pm 0.8 \text{ mol m}^{-2} \text{ dec}^{-1}$ lower compared to the first one (1994–2004: 12.1 ± 0.5 ; 2004–2014: $8.4 \pm 0.6 \text{ mol m}^{-2} \text{ dec}^{-1}$; $\pm 1\sigma$ uncertainty). In contrast, the mean ΔC_{ant} column inventory in the subtropical latitudes of the South Atlantic (20–50°S) is $4.7 \pm 2.2 \text{ mol m}^{-2} \text{ dec}^{-1}$ higher in the second decade (1994–2004: 8.5 ± 0.9 ; 2004–2014: $13.2 \pm 1.9 \text{ mol m}^{-2} \text{ dec}^{-1}$). In other regions of the ocean, the decadal differences are within or close to the bounds of the uncertainty of our estimates inferred from a set of alternative reconstructions. We thus refrain from further analysis. Overall, the spatial patterns in the decadal difference of our ΔC_{ant} column inventories are reminiscent of the anomaly structure that Gruber et al. (2019) derived from a comparison of their ΔC_{ant} column inventories to the steady-state projection of the total C_{ant} inventory in 1994 from Sabine et al. (2004).

3.2. Vertical Distribution

The high column inventories of ΔC_{ant} in the centers of the subtropical gyres seen in Figures 2a and 2b are due to a deeper penetration of ΔC_{ant} in these regions. This is illustrated by plotting ΔC_{ant} along a global section (Figures 3a and 3b) that connects the zonal mean sections of the Atlantic and Pacific Ocean with a meridional mean section crossing the Indian Ocean sector of the Southern Ocean. Within the subtropical gyres, ΔC_{ant} exceeding $5 \mu\text{mol kg}^{-1} \text{ dec}^{-1}$ reaches at least 300 m deeper than in the equatorial regions. This is primarily a consequence of the passive tracer transport of C_{ant} along isopycnal surfaces (depicted in Figure 3c), which brings C_{ant} more rapidly into the ocean's interior in regions of downward sloping isopycnals (Bopp et al., 2015; DeVries & Primeau, 2011). In the South Pacific, the ΔC_{ant} signal reaches deeper into the water column compared to the North Pacific, which is a persistent pattern for both decades and attributed to the formation of Subantarctic Mode and Antarctic Intermediate Water (SAMW and AAIW). In contrast, in the Atlantic Ocean we identify a shift

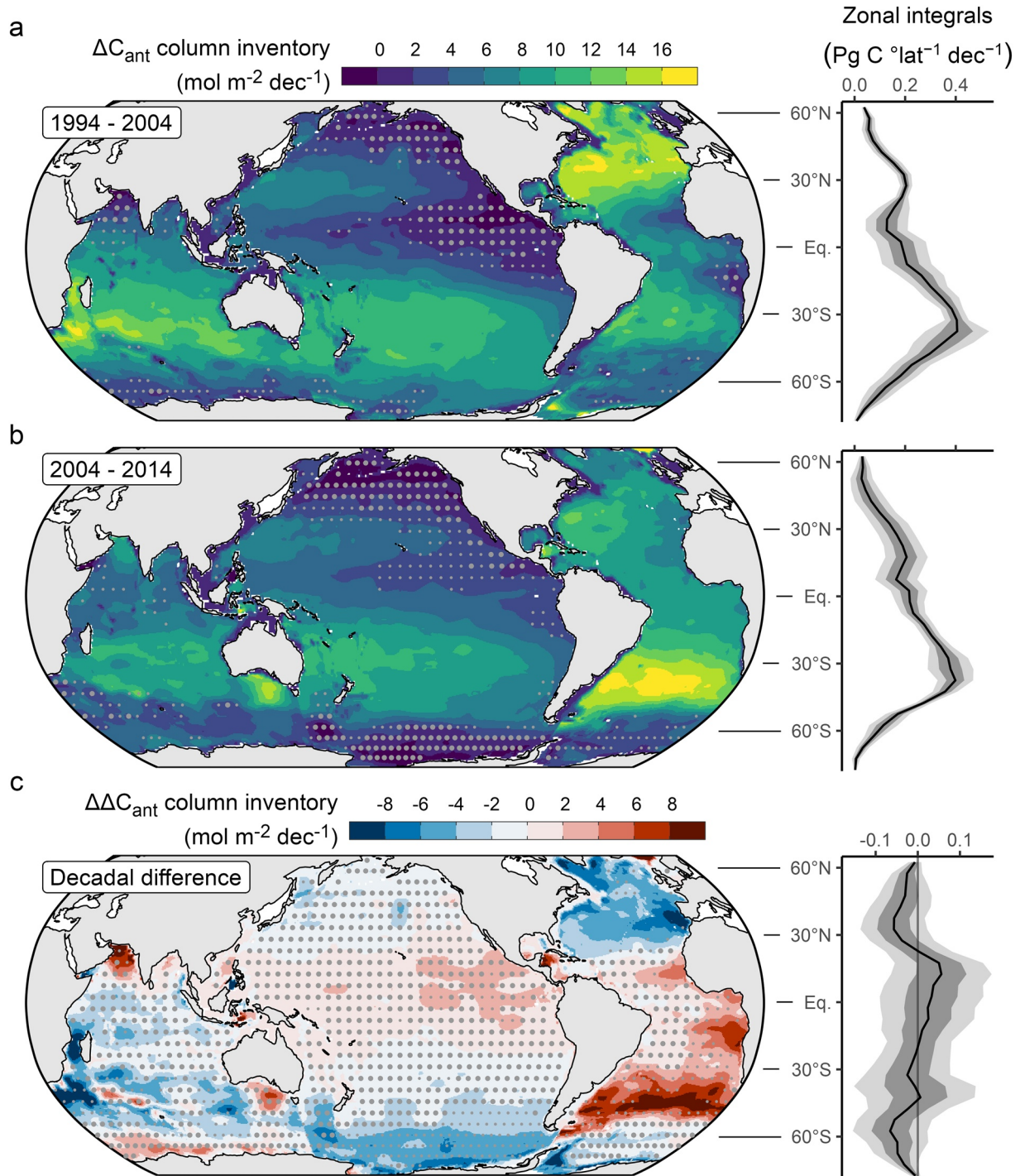


Figure 2. Column inventory maps and zonal integrals of the storage change of anthropogenic carbon (ΔC_{ant}) integrated over the upper 3,000 m of the ocean for (a) 1994–2004 and (b) 2004–2014. Decadal differences in the storage changes ($\Delta \Delta C_{ant}$) are shown in (c). Plotted here are the results from the standard configuration. Stippling on the maps with small/large dots indicates regions in which the column inventories are lower than the respective 2σ - 1σ -uncertainty. Likewise, shading around the zonal integrals represents the 1σ - and 2σ -uncertainty ranges.

of the deepest penetration of the ΔC_{ant} level of $5 \mu\text{mol kg}^{-1} \text{dec}^{-1}$ from the Northern to Southern Hemisphere (Figure 3c).

These changes in the downward extensions of ΔC_{ant} cause the decadal differences identified in the column inventories of ΔC_{ant} in the Atlantic Ocean (Figure 2c). The decrease of the mean ΔC_{ant} column inventory in the

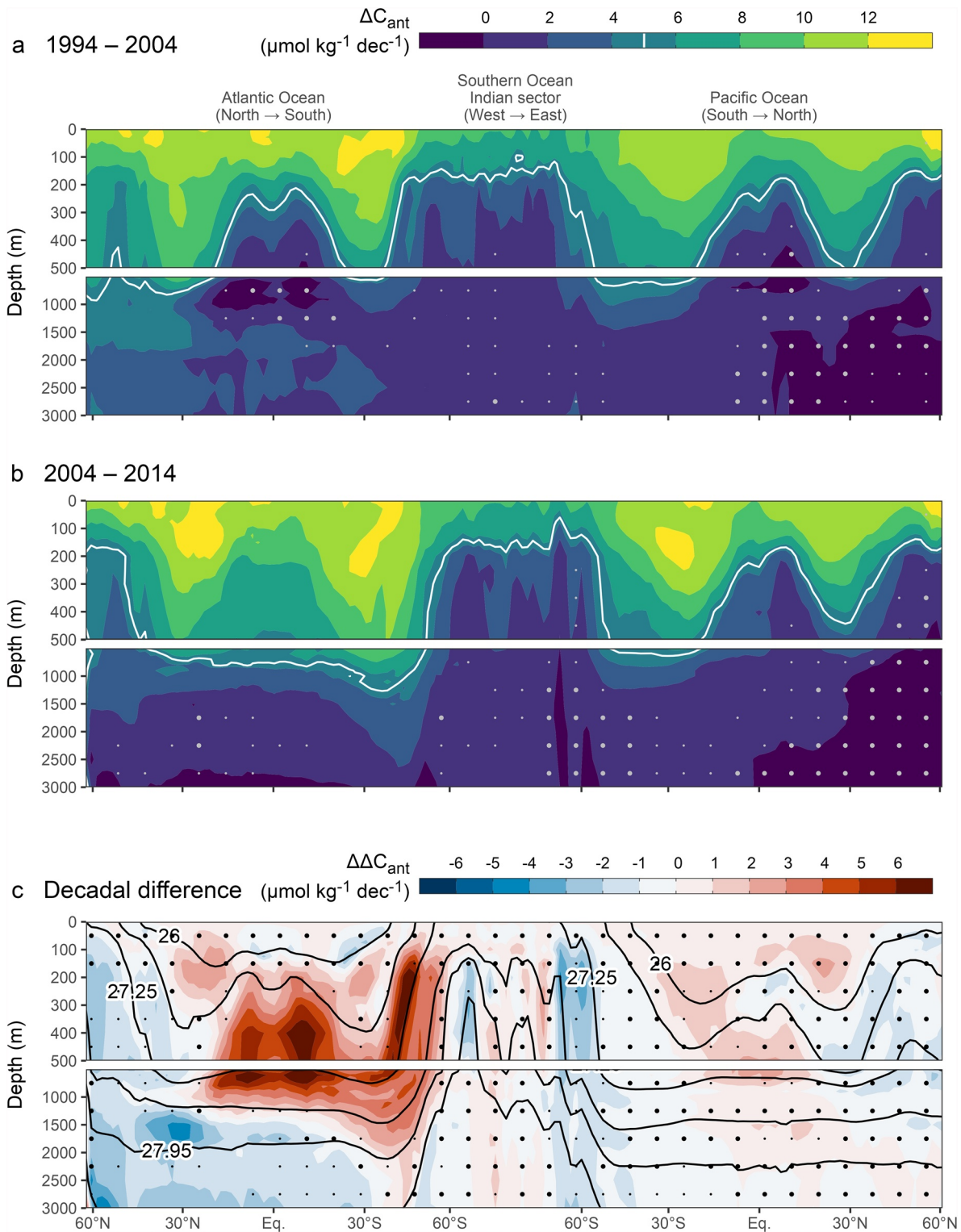


Figure 3. Global sections of changes in the anthropogenic carbon content from north to south in the Atlantic Ocean, west to east in the Southern Ocean and south to north in the Pacific Ocean. The standard case reconstruction of ΔC_{ant} is shown for the decades (a) 1994–2004 and (b) 2004–2014. The white contour lines highlight the ΔC_{ant} level of $5 \mu\text{mol kg}^{-1} \text{dec}^{-1}$. (c) Decadal differences between the storage changes ($\Delta\Delta C_{\text{ant}}$) shown in (a) and (b). Black contour lines in (c) indicate isoneutral density levels. The selected contours represent every second density slab used to cluster the data in the vertical dimension. Stippling with small or large dots indicates regions in which the ΔC_{ant} and $\Delta\Delta C_{\text{ant}}$ are lower than the 2σ - or 1σ -uncertainty, respectively. The North-South sections through the Atlantic and Pacific Ocean show zonal mean values across the entire basins, while the Southern Ocean sector is represented by a meridional mean section ranging from 55°S to 65°S that is compressed by a factor of 2.5 in distance. The location of the global section and areas for the computation of the zonal and meridional mean sections are displayed in Figure S1 in Supporting Information S1.

North Atlantic is a consequence of the weaker C_{ant} storage increase in the North Atlantic Deep Water (NADW), evident in the zonal mean section as negative decadal differences (-2 to $-5 \mu\text{mol kg}^{-1} \text{dec}^{-1}$) at neutral densities $>27.5 \text{ kg m}^{-3}$ (Figure 3c). In contrast, the decadal increase of the ΔC_{ant} column inventory in the South Atlantic can be attributed to an intensified rate of C_{ant} storage in the Subantarctic Mode Waters (SAMW) and Antarctic Intermediate Waters (AAIW). Here, positive ΔC_{ant} differences in the zonal mean sections are well confined to the neutral density slabs ranging from 26.5 to 27.5 kg m^{-3} (Figure 3c). The decadal ΔC_{ant} differences in the NADW and the AAIW are larger than the uncertainty of our reconstructions, while in most other water masses, the decadal differences are not significant (stippling in Figure 3c).

Examining the vertical distribution of the reconstructed ΔC_{ant} in terms of area-weighted mean content profiles (Figure 4a), we find that globally C_{ant} in the upper 50 m of the ocean increased on average by 10 – $11 \mu\text{mol kg}^{-1} \text{dec}^{-1}$ in both decades. As the storage change near the surface is determined based on an assumed equilibrium with the atmospheric CO_2 , it shows latitudinal patterns that reflect gradients in the surface ocean buffer capacity (Figures 3a and 3b). However, regional differences of the surface ΔC_{ant} averaged over hemispheric ocean basins are small (Figure 4a). Furthermore, the almost identical surface ΔC_{ant} for both decades is due to a compensation of the higher atmospheric CO_2 growth rate and the reduced surface ocean buffer capacity in the second decade of our analysis. In contrast to the rather steady accumulation of C_{ant} in the surface ocean, the decadal differences in the mean ΔC_{ant} profiles tend to be more pronounced at depth in some regions. In the North Atlantic, ΔC_{ant} below 1000 m is about $3 \mu\text{mol kg}^{-1} \text{dec}^{-1}$ lower during the second decade (Figure 4a), while the mean ΔC_{ant} signal in the South Atlantic was significantly higher by about $3 \mu\text{mol kg}^{-1} \text{dec}^{-1}$ between 500 and 1500 m during the second decade.

3.3. Regional and Global Inventories

Reflecting the rapid decrease of ΔC_{ant} with depth (Figure 4a), almost 50% of the global C_{ant} storage change occurs in the upper 500 m of the water column (Figure 4b). Over the upper 1,000 m, this share increases to around 75%, except in the North Pacific, where the entire inventory increase is fully confined to the top 1,000 m. In all other ocean regions depicted in Figure 4b, a significant fraction of the C_{ant} storage change occurs below 1,000 m ($\sim 25\%$ on a global basis) as a result of the more rapid water mass transport and mixing between the surface and ocean interior in these regions. The decadal differences in the ΔC_{ant} inventories for 500 m depth layers reflect the profiles of the amount content and were found to be significant only in the three depth layers below 1500 m of the North Atlantic, as well as between 500 and 1,500 m in the South Atlantic (Figure 4b).

Once integrated over the top 3,000 m of entire ocean basins (Figure 5 and Table 1), the South Pacific stands out as the region with the highest increase of C_{ant} storage for both decades (1994–2004: $8.6 \pm 1.2 \text{ Pg C dec}^{-1}$ and 2004–2014: $7.4 \pm 1.0 \text{ Pg C dec}^{-1}$), followed by the Indian Ocean (7.2 ± 0.9 and $5.7 \pm 0.6 \text{ Pg C dec}^{-1}$). In contrast, the North Pacific accounts for the smallest contribution to the increase in the oceanic storage of C_{ant} in both decades (2.9 ± 0.8 and $3.2 \pm 1.8 \text{ Pg C dec}^{-1}$). The decadal differences in the increases in C_{ant} storage are not significant at the 2σ -uncertainty level in any of these three regions. This is different for the North Atlantic (Figure 5, Table 1), which represented the third largest sink region during the 1994–2004 decade ($4.8 \pm 0.2 \text{ Pg C dec}^{-1}$), but experienced a C_{ant} accumulation rate that was significantly reduced by $0.9 \pm 0.4 \text{ Pg C dec}^{-1}$ during the 2004–2014 period ($3.9 \pm 0.4 \text{ Pg C dec}^{-1}$). In contrast, the storage rate in the South Atlantic increased by $1.5 \pm 0.8 \text{ Pg C dec}^{-1}$ from the first ($3.9 \pm 0.5 \text{ Pg C dec}^{-1}$) to the second decade ($5.4 \pm 0.6 \text{ Pg C dec}^{-1}$) of our analysis. As a consequence, the South Atlantic represents the third largest contributor to the global accumulation of C_{ant} from 2004 to 2014. The ranking of the ocean basins in terms of their contribution to the global ocean C_{ant} sink reflects primarily the differences in surface area of the basins.

The ranking of the regions changes markedly in terms of the area-normalized storage sensitivity β_{area} (Table 1 and Figures S4 and S5 in Supporting Information S1), which is a measure of how much additional C_{ant} the ocean is storing within any given region in response to the increase in atmospheric CO_2 (see Section 2.4). The North Atlantic has the highest regional storage sensitivity (25%–40% larger than the global mean), and the North Pacific the lowest one (about 45%–55% lower than the global mean). This largely reflects the differences in intermediate, mode, and deep water formations between the different basins, and will be further discussed in Section 4.1.

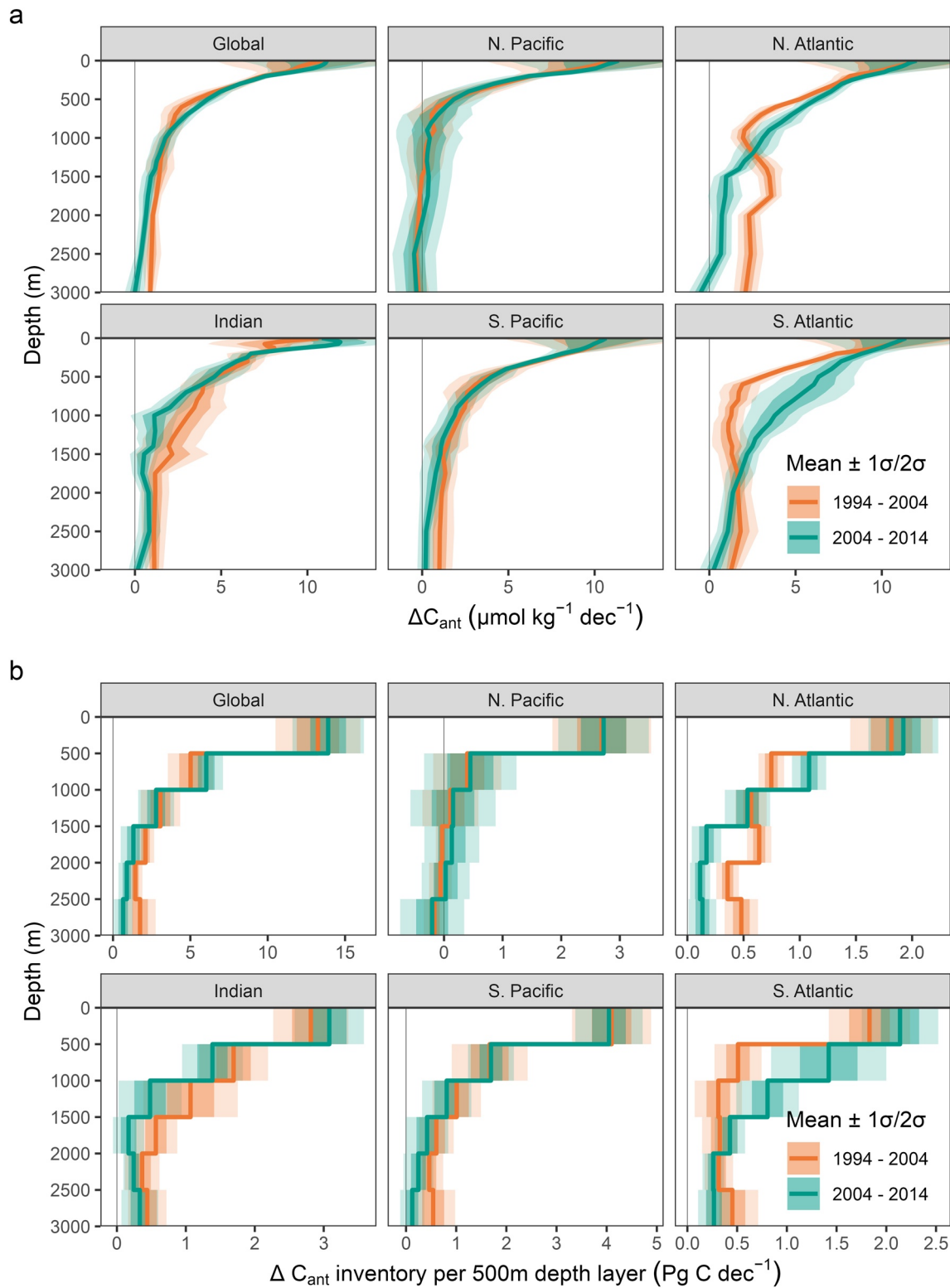


Figure 4. Mean vertical distribution of the decadal changes in anthropogenic carbon (ΔC_{ant}) for the global ocean and both hemispheres of the main ocean basins: (a) mean content profiles and (b) 500-m-depth layer inventories of ΔC_{ant} . Colors distinguish the decades 1994–2004 and 2004–2014. Thick lines represent the standard case reconstruction of ΔC_{ant} and ribbons indicate the 1σ - and 2σ -uncertainty ranges.

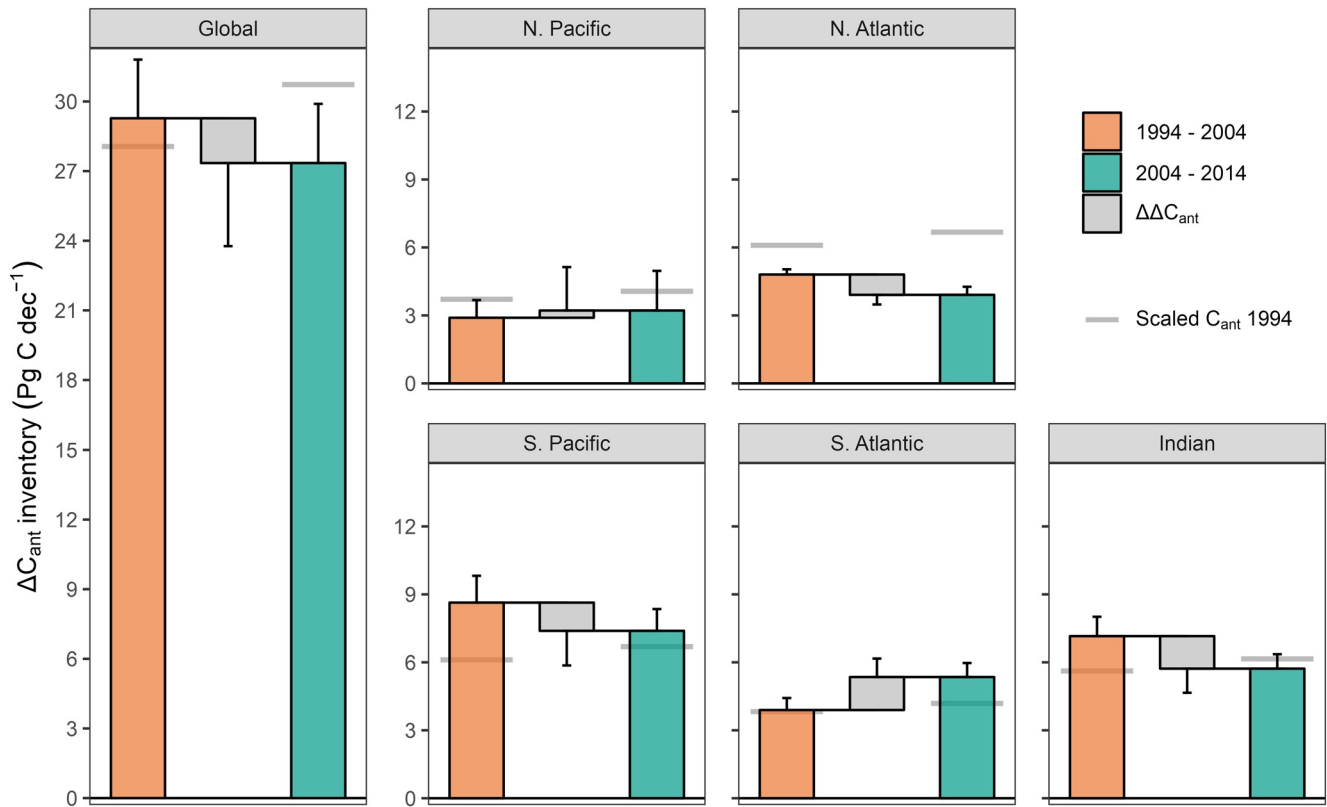


Figure 5. Change in the storage of anthropogenic carbon (ΔC_{ant} inventory) integrated over the top 3,000 m of the global ocean (left panel) and each hemisphere of the main ocean basins (right panels). Colored bars depict the inventory changes for the decades 1994–2004 and 2004–2014, and gray bars represent the decadal difference ($\Delta\Delta C_{\text{ant}}$ inventory). Error bars displayed in the direction of change represent the 1σ -uncertainty of each estimate. Horizontal lines indicate projected inventory changes based on the total C_{ant} storage in 1994 (Sabine et al., 2004) and assuming proportional growth with atmospheric CO_2 (see text for details).

When integrating ΔC_{ant} globally and scaling it for unmapped regions and deep water storage, we determine an ocean sink for anthropogenic CO_2 that amounts to 29.3 ± 2.5 and $27.3 \pm 2.5 \text{ Pg C dec}^{-1}$ for the 1994–2004 and the 2004–2014 decade, respectively (Figure 5, Table 1). These inventory changes of C_{ant} are indistinguishable for both decades with a difference of $-1.9 \pm 3.6 \text{ Pg C dec}^{-1}$, indicating that the global ocean continued to act as a strong sink for anthropogenic CO_2 in the recent past. The global area-normalized storage sensitivity β_{area} decreased markedly and significantly, however, from $0.37 \pm 0.03 \text{ mol m}^{-2} \text{ ppm}^{-1}$ for the decade 1994–2004 to $0.31 \pm 0.03 \text{ mol m}^{-2} \text{ ppm}^{-1}$ during the second decade 2004–2014 (Table 1), suggesting a slowdown of the global ocean C_{ant} uptake relative to what one would expect on the basis of the growth in atmospheric CO_2 . For the 20-year period from 1994 to 2014, the directly estimated global ΔC_{ant} inventory is identical to the sum of the estimates from the individual decades ($56.7 \pm 3.5 \text{ Pg C dec}^{-1}$).

3.4. Uncertainty Assessment

Nearly all identified main configuration choices of the eMRL(C^*) method matter for the reconstruction of the decadal increases in C_{ant} and contribute to the uncertainties of the global inventory changes of about $\pm 10\%$ (Table 1, Figure 6; Figures S9 and S10 in Supporting Information S1). The smallest uncertainty contributions stem from alternative definitions of C^* and from uncertainties associated with the predictor climatologies used for mapping (Figure 6). All other configuration choices matter more, although differently for the two decades, largely reflecting differences in the data distribution and data consistency.

The single largest contribution to the global inventory uncertainty comes from the way we applied the adjustments to the DIC, TA, and PO_4^{3-} measurements in order to ensure the highest level of data consistency. If the adjustments were determined and applied separately for each cruise instead of in a bulk manner as done in the standard configuration, the global ΔC_{ant} inventories change by $\sim -0.5 \text{ Pg C dec}^{-1}$ during the 2004–2014 period,

Table 1
Inventories of the Change in Anthropogenic Carbon Storage (ΔC_{ant} Inventory) for the First (1994–2004) and Second (2004–2014) Decade of Our Analysis, Integrated Separately Across Both Hemispheres of the Main Ocean Basins and the Global Ocean. The Inventory Changes are Further Related to the Decadal Growth Rates in Atmospheric CO_2 ($\Delta \text{CO}_{2,\text{atm}}$) to Derive the Sink Sensitivity β in Absolute Terms ($\beta = \text{Inv}(\Delta C_{\text{ant}})/\Delta \text{CO}_{2,\text{atm}}$) and Normalized to the Surface Area (A) of Each Ocean Basin ($\beta_{\text{area}} = \beta/A$ in $\text{mol m}^{-2} \text{ppm}^{-1}$).

Parameter (unit)	Region (area in 10^6 km^2)	1994–2004	2004–2014	Decadal difference
ΔC_{ant} inventory (Pg C dec^{-1})	Global	29 ± 2.5	27 ± 2.5	-1.9 ± 3.6
	N. Pacific	2.9 ± 0.8	3.2 ± 1.8	0.3 ± 1.9
	S. Pacific	8.6 ± 1.2	7.4 ± 1.0	-1.2 ± 1.5
	N. Atlantic	4.8 ± 0.2	3.9 ± 0.4	$-0.9 \pm 0.4^{**}$
	S. Atlantic	3.9 ± 0.5	5.4 ± 0.6	$1.5 \pm 0.8^*$
	Indian	7.2 ± 0.9	5.7 ± 0.6	$-1.4 \pm 1.1^*$
$\Delta \text{CO}_{2,\text{atm}}$ (ppm dec^{-1})	Global	18.6	20.4	1.8
β (Pg C ppm^{-1})	Global ^a	1.6 ± 0.1	1.3 ± 0.13	$-0.23 \pm 0.18^*$
β_{area} ($\text{mol m}^{-2} \text{ppm}^{-1}$)	Global ^a (333)	0.37 ± 0.03	0.31 ± 0.03	$-0.05 \pm 0.04^*$
	N. Pacific (76)	0.17 ± 0.05	0.17 ± 0.09	0.002 ± 0.1
	S. Pacific (96)	0.40 ± 0.06	0.31 ± 0.04	$-0.09 \pm 0.07^*$
	N. Atlantic (41)	0.53 ± 0.03	0.39 ± 0.04	$-0.14 \pm 0.04^{**}$
	S. Atlantic (45)	0.39 ± 0.05	0.49 ± 0.06	$0.1 \pm 0.08^*$
	Indian (73)	0.44 ± 0.05	0.32 ± 0.04	$-0.12 \pm 0.06^*$

^aFor consistency with the regional estimates, the global β_{area} estimate is based on the directly mapped ΔC_{ant} inventory, whereas the global β estimate corresponds to the global ΔC_{ant} inventory as given in this table, obtained by scaling the mapped inventory to global coverage. All values refer to the standard cases of our ΔC_{ant} reconstruction and the corresponding 1σ -uncertainty ranges. Decadal differences are tagged with ** or * when they exceed the combined 2σ - or 1σ -uncertainty of both decades, respectively.

and by $\sim +1.5 \text{ Pg C dec}^{-1}$ for the 2004–2014 period. Nearly all of the changes during the earlier decade originate at the Indian Ocean, while those for the second period originate at the North Pacific (Figure 6; Figure S9 in Supporting Information S1), as expected given that these were the regions where we applied these adjustments.

The second most important uncertainty contribution comes from the regional clustering of the observations with uncertainty contributions to the regional inventories ranging from 0.2 to 0.8 Pg C dec^{-1} (Figure 6; Figure S9 in Supporting Information S1). However, for the global ΔC_{ant} inventories, the uncertainties arising from the regional clustering partially cancel out, such that the global uncertainty contribution is lower than the sum of the uncertainties in the individual basins ($<1.5 \text{ Pg C dec}^{-1}$ for both decades, Figure 6).

Among the other choices, the approach for the surface ΔC_{ant} reconstruction contributes about 1 Pg C dec^{-1} to the uncertainty of the global ΔC_{ant} inventory, determined by comparing our estimate based on the assumption of surface ocean equilibrium of C_{ant} with a reconstruction based on observation-based surface changes of DIC from OceanSODA (Gregor & Gruber, 2021). Choices associated with the gap filling also contribute about 1 Pg C dec^{-1} to the global uncertainty, but this error source is limited largely to the first decade and the South Pacific (Figure S9 in Supporting Information S1), where we had to include a substantial number of cruises that took place in the 1990s and provided only calculated TA data (Figure 1). Finally, our scaling of the ΔC_{ant} inventories for unmapped regions and the deep ocean introduces an additional uncertainty contribution of about 1 Pg C dec^{-1} , however, confined to the global ΔC_{ant} inventories and of very similar magnitude for both decades.

In addition to investigating the contribution of the configuration choices to the uncertainty of our standard configuration, we also determined the sensitivity of our results to a set of additional decisions we had to take for our reconstructions (see Text S4.2 in Supporting Information S1). We did not add these results to our formal uncertainty estimate since we consider our choices as well justified, and the alternatives as clearly inferior choices. Among all these additional decisions, we find that the biggest sensitivity of the results is associated with the

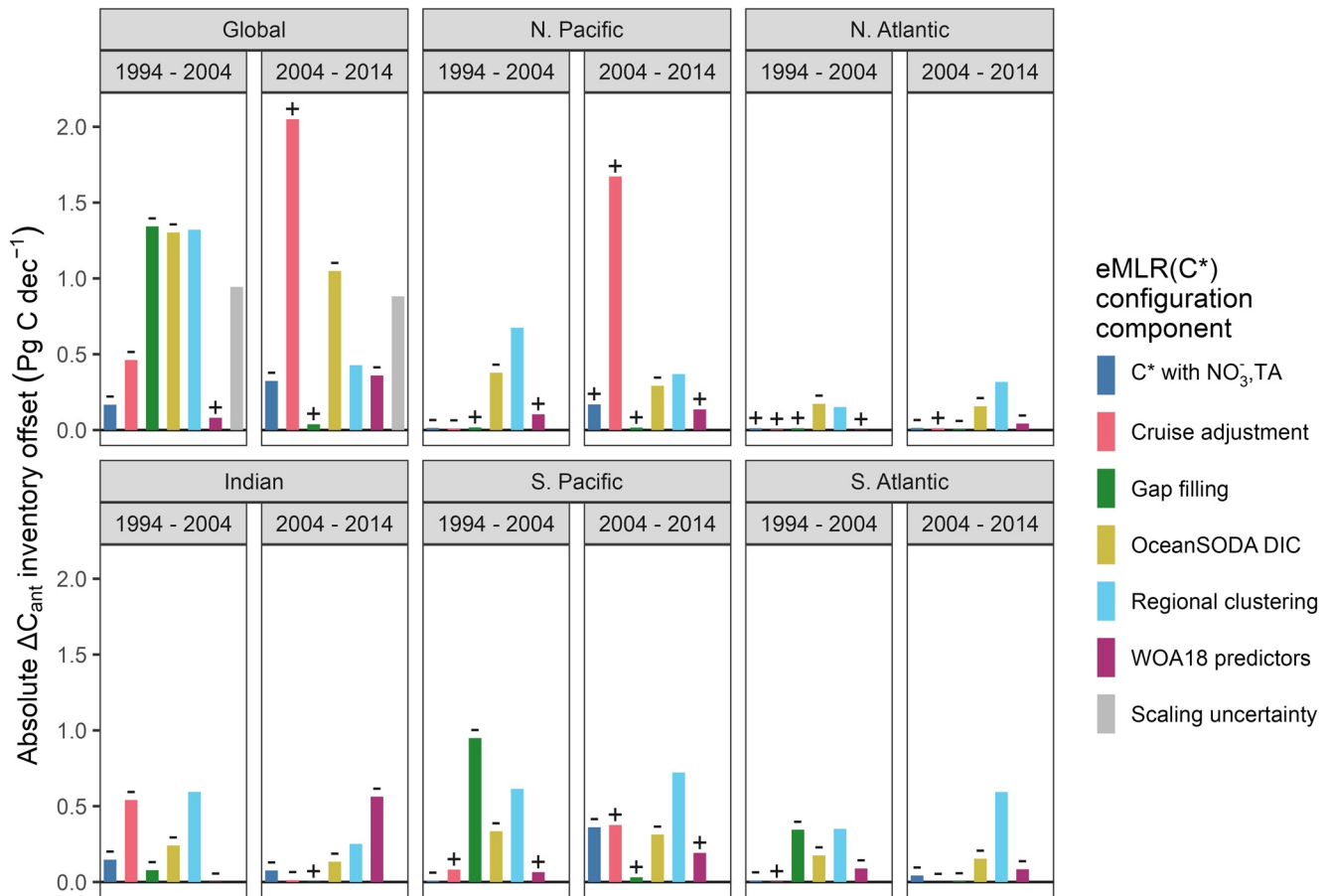


Figure 6. Inventory uncertainty contributions at the 1σ -uncertainty level determined as offsets between our standard case reconstruction and six configuration choices of the eMLR(C*) method (colors) for each ocean region and both decades (panels). All offsets are shown as absolute values. Where applicable, + or – symbols on top of each bar indicate that higher or lower inventory changes, respectively, were obtained when the configuration change was applied. The uncertainty contribution that accounts for our upscaling for unmapped water masses is shown for the global inventory.

data adjustments in the North Pacific. Our reconstructions based on the unadjusted data reveal that the ΔC_{ant} inventory in the North Pacific for the 2004–2014 period would be about 4 Pg C dec^{-1} higher than the standard case reconstruction (Figures S11 and S12 in Supporting Information S1) that includes the adjustments. Hence, the global ΔC_{ant} inventory in the last decade would be higher than that obtained for the 1994–2004 period without North Pacific data adjustment. As a consequence, the growth of the C_{ant} inventory in the last decade would be roughly proportional to growth in atmospheric CO_2 , such that we would interpret the storage sensitivity as unchanged over both decades and the industrial period. While multiple lines of evidence suggest that our data adjustments are justified and reflect inter-decadal measurement inconsistencies, the relevance of these adjustments for the interpretation of trends in the ocean carbon sink underpin the importance of long-term consistent ocean observations. Furthermore, we tested the sensitivity of our results to data coverage by reconstructing ΔC_{ant} with observations only from cruise sections that were reoccupied during both sampling periods. This reoccupation filter has generally a low impact on the reconstructed column inventories and basin inventories (Figures S11 and S12 in Supporting Information S1), suggesting an overall sufficient data coverage. An exception to this are the ΔC_{ant} reconstructions in the Indian Ocean, which are more sensitive to the reoccupation filter (Figure S11 in Supporting Information S1) due to the lack of data from the Arabian Sea during the central sampling period, that is, the 2000s (Figure 1b).

Our observation-based uncertainty and sensitivity findings are corroborated by our tests with synthetic data generated from an ocean hindcast model (Text S5 in Supporting Information S1), following the approach developed by Clement and Gruber (2018). Comparing the biases of our reconstructed model inventories to the estimated uncertainty based on the configuration choices, we find that the bias of 7 (11) out of 12 reconstructed

ΔC_{ant} inventories is within the 1σ - (2σ -) uncertainty range (Figure S18 in Supporting Information S1), which meets the expectation of a 68% (95%) confidence interval. Our uncertainty ranges and confidence intervals are thus considered suitable criteria to evaluate the significance of our ΔC_{ant} reconstructions. Furthermore, the eMLR(C^*) method proves capable of reconstructing the global ΔC_{ant} patterns (Figure S13 in Supporting Information S1). The reconstruction biases of the ΔC_{ant} column inventories are below $2 \text{ mol m}^{-2} \text{ dec}^{-1}$ for 87% of the total ocean surface area, within $2\text{--}4 \text{ mol m}^{-2} \text{ dec}^{-1}$ for 13%, and only exceed the latter threshold for $<0.5\%$ of the surface area. In contrast, the true ΔC_{ant} column inventories in our model are larger than these thresholds of 2 and $4 \text{ mol m}^{-2} \text{ dec}^{-1}$ over more than 90% and 55% of the surface area of the ocean, respectively (Figure S13a in Supporting Information S1). In agreement with this assessment based on synthetic data, the observation-based ΔC_{ant} column inventories exceed the 1σ - and 2σ -uncertainty level over more than 90% and 75% of the total ocean surface area (Figure 2a). ΔC_{ant} column inventories that are lower than the local uncertainty are confined to regions with low ΔC_{ant} column inventories, primarily in the North Pacific (Figure 2a). We conclude that the global distribution patterns of ΔC_{ant} are robustly reconstructed, which is in line with previous assessments of the method (Clement & Gruber, 2018) despite the shorter sampling periods applied in this study.

The tests with synthetic data subsampled from a GOBM are useful to demonstrate the skill of the eMLR(C^*) method to reconstruct the inventory and spatial patterns of ΔC_{ant} . However, the tendency of the GOBMs to simulate a lower decadal variability of the ocean carbon sink compared to observation-based surface CO_2 flux products (Hauck et al., 2020) suggest that this testing approach may not be well suited to investigate the method's ability to detect decadal differences in the C_{ant} storage rates ($\Delta\Delta C_{\text{ant}}$). As a consequence of the model's low decadal variability, the spatial patterns in the column inventory biases show a strong correlation with the reconstructed $\Delta\Delta C_{\text{ant}}$ (Figures S14 and S15 in Supporting Information S1). However, the observation-based $\Delta\Delta C_{\text{ant}}$ column inventories in the Atlantic Ocean (Figure 2b) are higher than the $\Delta\Delta C_{\text{ant}}$ biases in the tests with synthetic data by about a factor of two (Figure S15 in Supporting Information S1), suggesting that the observation-based $\Delta\Delta C_{\text{ant}}$ patterns carry, at least in part, a true signal.

3.5. Comparison With Regional Estimates

As a final component to assess the robustness of our estimates, we compare our ΔC_{ant} reconstructions to previous regional estimates that—same as our study—resolve changes for at least two periods and apply an MLR approach to ocean interior observations (see Text S6 in Supporting Information S1 for details). Regional studies that fulfill these criteria are available for the North and South Atlantic (Gao et al., 2022; Wanninkhof et al., 2010; Woosley et al., 2016), as well as the North and South Pacific (Carter et al., 2019), but not for the Indian Ocean (Murata et al., 2010; Sabine et al., 1999). We conclude from this comparison that the magnitude, patterns and trends in our ΔC_{ant} reconstructions agree with those determined in regional studies, and that differences can—where they exist—be attributed to differences in the chosen integration depth, differences in the definition of the target variable C^* , and sometimes also to the uncertainty associated with the computation of a whole basin inventory from a single reoccupied transect (Gao et al., 2022; Woosley et al., 2016).

The most pronounced difference to a regional estimate exists in the South Pacific, where Carter et al. (2019) determined a change of the C_{ant} inventory of $5.4 \pm 0.6 \text{ Pg C dec}^{-1}$ from 1995 to 2005, whereas we determine a substantially higher inventory change of $8.6 \pm 1.2 \text{ Pg C dec}^{-1}$ for almost the same period (1994–2004). A main difference between these studies is the calculation of C^* without (Carter et al., 2019) or with (this study) a TA contribution. Our sensitivity reconstruction of ΔC_{ant} in the South Pacific without considering the contribution of TA for the calculation of C^* indeed reveals an inventory change that is about 3 Pg C dec^{-1} lower than our standard case reconstruction. Carter et al. (2019) relied on a synthetic data sensitivity test that included synthetic measurement uncertainties to conclude that the eMLR results are more robust for their implementation when the TA adjustment is omitted from the C^* calculation. However, methodological differences between the methods used in that and our study limit the applicability of their sensitivity tests for our approach. We further contend that the additional attention paid to TA quality control results in better TA consistency between cruises than is assumed by Carter et al. (2019) and that the possibility of DIC changes driven by the calcium carbonate cycle (that are neither well represented in the synthetic data nor sufficiently correlated with nutrient and oxygen changes that they would be removed by following the eMLR approach) should not be neglected.

The second largest difference from a regional ΔC_{ant} inventory exists in the North Atlantic Ocean, where Wanninkhof et al. (2010) determined a C_{ant} storage rate of only $1.9 \pm 0.4 \text{ Pg C dec}^{-1}$ for the 1993–2003 period

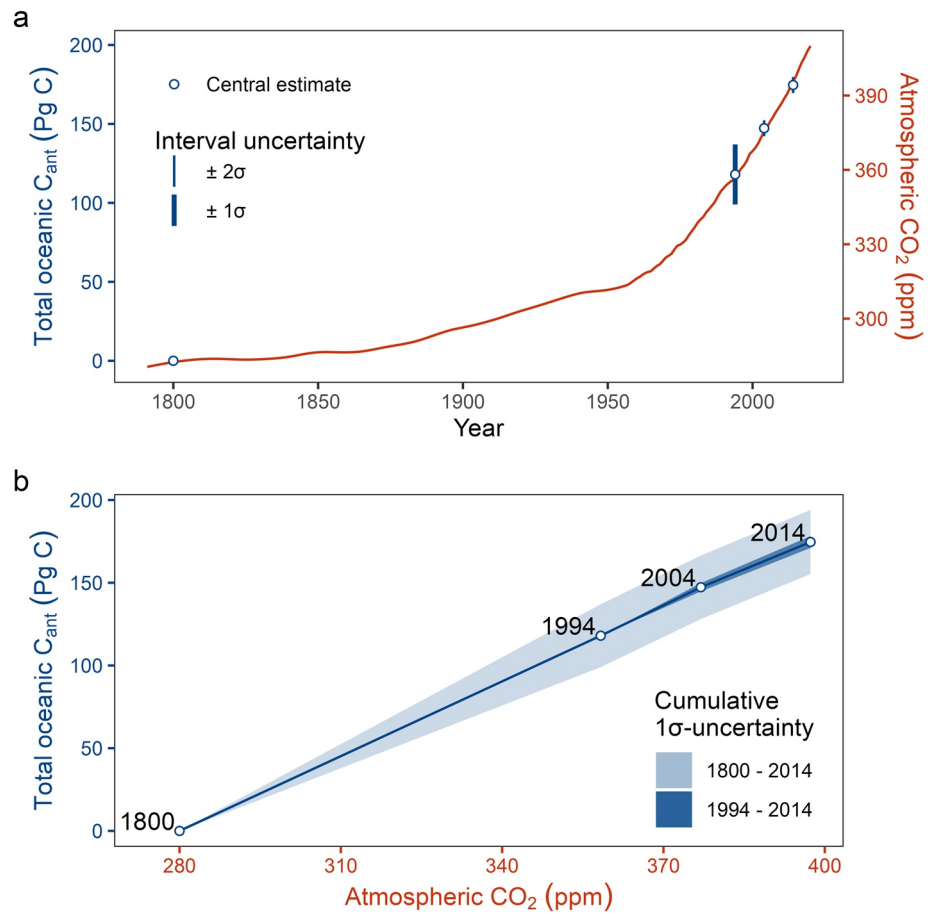


Figure 7. Total C_{ant} accumulation in the ocean interior from 1800 to 2014, shown in blue as a function of (a) time and (b) atmospheric CO_2 . Total C_{ant} was estimated by adding our global C_{ant} inventory changes (Table 1) to the total C_{ant} inventory in 1994 (118 ± 19 Pg C) according to Sabine et al. (2004). The red line in (a) shows the time history of atmospheric CO_2 . The cumulative uncertainty in (b) for the 1994–2014 period (dark blue ribbon) assumes zero uncertainty in 1994.

based on a single reoccupied cruise section. Their estimate is drastically lower than ours for the 1994–2004 decade (4.8 ± 0.2 Pg C dec^{-1}). Our tests of the eMLR(C^*) method reveal that the uncertainty of our estimates can only explain a minor part of this offset. We conclude that the offset is primarily due to differences in the integration depth, structural uncertainties in the regional estimate (Wanninkhof et al., 2010) and extrapolation errors from a single reoccupied cruise section to a whole basin inventory. In fact, Woosley et al. (2016) found that the whole basin inventories of the North Atlantic differ by $\sim 30\%$ when comparing estimates obtained from a single section to those obtained from three sections.

In general, the individual differences between our regional ΔC_{ant} inventories and those obtained in the previous regional studies are within the uncertainty range of our global inventory. Therefore, we do not assume that offsets at the regional scale challenge the robustness and interpretation of our global inventories.

4. Discussion

4.1. Decadal Trends or the Ocean at a Time of Change

Our ocean-interior observation-based reconstruction of the changes in the global oceanic storage of anthropogenic carbon reveals for the two consecutive decades since 1994 indistinguishable accumulation rates, that is, 29.3 ± 2.5 Pg C dec^{-1} and 27.3 ± 2.5 Pg C dec^{-1} for 1994–2004 and 2004–2014, respectively (Figure 5, Table 1). Putting this continued accumulation of anthropogenic carbon into the context of the total oceanic C_{ant} storage in 1994 (118 ± 19 Pg C), we confirm the expected linear correlation with the increase in atmospheric CO_2 (Figure 7, see also Gruber et al., 2023). But for a more detailed and quantitative discussion of the recent decadal trends in the

ocean carbon sink, it is informative to look at potential changes in the slope of this relationship, that is, changes in the global sensitivity β and the associated area-normalized sensitivity β_{area} (see Section 3.3). For the global sensitivity β , we compute values of $1.6 \pm 0.1 \text{ Pg C ppm}^{-1}$ and $1.3 \pm 0.1 \text{ Pg C ppm}^{-1}$ for the two decades, respectively (Table 1, Figure 7). Their average confirms the long-term mean value of $1.4 \pm 0.1 \text{ Pg C ppm}^{-1}$ diagnosed by Gruber et al. (2023), but the significant decrease of about $15 \pm 11\%$ between the two decades indicates a weakening of the ocean sink for C_{ant} . The reason that this difference in β is significant, while the $7 \pm 12\%$ reduction ($-1.9 \pm 3.6 \text{ Pg C dec}^{-1}$) in the global ΔC_{ant} inventory is not, is due to the $\sim 10\%$ higher growth rate in atmospheric CO_2 from 2004 to 2014 compared to that during the previous decade (Table 1).

As the ocean acidifies in response to taking up CO_2 , a decrease of the ocean sink efficiency is expected due to the decrease of the ocean buffer capacity (Jiang et al., 2019). Over the past 40 years, seawater that followed the same pCO_2 increase as the atmosphere would have experienced a $\sim 6\%$ reduction of the DIC increase per change in pCO_2 roughly every 10 years. This estimate is based on fundamental marine CO_2 -system considerations and reflects an increase in the Revelle factor (Sarmiento & Gruber, 2006). The 6% decadal weakening of the ability of the surface ocean carbonate chemistry to buffer the increase in pCO_2 can explain about half of the observed decrease in the sink sensitivity β . The other half is most likely attributable to changes in the ocean's circulation and upper ocean stratification (Sallée et al., 2021) that appears to have led to a less efficient downward transport of C_{ant} , which we discuss further in the following.

Roughly half of the decrease of the global ocean carbon sink stems from the reduced decadal storage changes in the North Atlantic ($-0.9 \pm 0.4 \text{ Pg C dec}^{-1}$). Here, we find a significant weakening of the area-normalized sink sensitivity β_{area} ($-0.14 \pm 0.04 \text{ mol m}^{-2} \text{ ppm}^{-1}$) when comparing the first (1994–2004) to the second decade (2004–2014) of our analysis (Table 1, Figures S4 and S5 in Supporting Information S1). Furthermore, our β_{area} estimates for both decades are well below that obtained for the 1800–1994 period (Sabine et al., 2004), indicating a progressive weakening of the sink efficiency in the North Atlantic. The most plausible explanation for this progressive weakening is a tendency of the Atlantic Meridional Overturning Circulation (AMOC) to weaken since the 1980s (Jackson et al., 2019, 2022; Latif et al., 2022). Attributing the decadal ΔC_{ant} differences to changes in AMOC strength is supported by the localization of the negative $\Delta \Delta C_{\text{ant}}$ signal in the North Atlantic Deep Water (Figure 3c). This view is also in line with two previous sets of regional studies: (a) Pérez et al. (2010, 2013) found that the C_{ant} storage rates in the North Atlantic subpolar gyre during the phase of a low North Atlantic Oscillation (NAO) from 1997 to 2006 were $\sim 48\%$ lower than those during the first half of the 1990s, when a high NAO phase was dominant, although the mechanistic processes linking the NAO, subpolar convection strength, gyre circulation and the AMOC are not yet fully understood. (b) Raimondi et al. (2021) reconstructed C_{ant} column inventories in the Central Labrador Sea based on CFC-12 observations and identified a period of near zero C_{ant} increases between 2003 and 2012.

However, an important caveat regarding our finding of a progressively weakening North Atlantic C_{ant} sink is the fact that the available ocean interior observations in the North Atlantic stem mostly from the first half of our last sampling period, the 2010s. However, after 2013 the NAO switched to a strong positive phase (Holliday et al., 2020) and in line with this, the C_{ant} column inventories in the Central Labrador Sea rapidly increased (Raimondi et al., 2021). Likewise, a deep convection event in the Irminger Sea in winter 2014/15 injected anthropogenic carbon into the ocean interior and almost tripled the storage rates compared to those determined from previous hydrographic sections (Fröb et al., 2016). It is thus possible that our reconstructions do not capture a very recent reinvigoration of the North Atlantic C_{ant} sink, due to the temporal distribution of the available observations.

The decadal difference of the South Atlantic C_{ant} sink is significant at the 1σ -uncertainty level ($+1.5 \pm 0.8 \text{ Pg C dec}^{-1}$) and slightly exceeds the increase expected from the growth in atmospheric CO_2 alone, expressed in an increase of the sink sensitivity ($+0.1 \pm 0.08 \text{ mol m}^{-2} \text{ ppm}^{-1}$). In contrast to the North Atlantic, the decadal change in the South Atlantic is not of progressive nature when putting it into context of the total C_{ant} storage until 1994 (Figure 5), that is, only the second decade reveals a tendency toward an elevated storage sensitivity. Due to the strong spatial coherence between the positive $\Delta \Delta C_{\text{ant}}$ signal and the Subantarctic Mode and Antarctic Intermediate Waters (Figure 3c), we attribute the decadal differences found in the South Atlantic to increased ventilation rates of these water masses (DeVries et al., 2017; Panassa et al., 2018; Patara et al., 2021; Shi et al., 2021).

Although the decadal inventory changes in the Indian Ocean and South Pacific are much less robust than those in the Atlantic, they represent in sum a contribution of about $2.6 \pm 1.9 \text{ Pg C dec}^{-1}$ to the decline of the global

inventory. As the negative $\Delta\Delta C_{\text{ant}}$ signals in these regions are associated primarily with Antarctic Bottom Water and Lower Circumpolar Deep Waters (Figure S7 in Supporting Information S1), the decadal differences in the C_{ant} storage changes are likely a consequence of circulation changes as well, albeit determined with lower uncertainty than in other regions.

An additional, and globally perhaps more uniform, contribution to the decrease may stem from the observed increase in upper ocean stratification (Sallée et al., 2021). Sallée et al. found that the density contrast across the base of the mixed layer had increased by about 9% per decade between 1970 and 2018. Although their estimate pertains only to the summer, such an increase in stratification is bound to decrease the transport of C_{ant} from the surface to depth, that is, the most important bottleneck for the uptake of C_{ant} from the atmosphere.

We conclude that in addition to the decrease of the ocean buffer capacity, ocean circulation changes and the increase in stratification are likely to play an important role in driving the decrease in the sink sensitivity, that is, the strength of the oceanic sink for anthropogenic carbon per unit change in atmospheric CO_2 .

4.2. Comparison With Observation-Based Surface Flux Estimates: Implications for Changes in the Natural Carbon Storage

In the following, we compare our estimates of the global oceanic sink of anthropogenic carbon to an ensemble of observation-based surface CO_2 flux products assembled by the Global Carbon Budget (Friedlingstein et al., 2022). During the 1994–2004 decade, the ocean interior accumulation of anthropogenic carbon ($29.3 \pm 2.5 \text{ Pg C dec}^{-1}$) exceeds the time-integrated net air-sea flux of CO_2 of $21.4 \pm 2.8 \text{ Pg C dec}^{-1}$ (Figure 8 and Table 2). For this comparison, we followed GCB procedures and adjusted the observation-based air-sea fluxes for a preindustrial steady-state outgassing of riverine CO_2 of $6.1 \text{ Pg C dec}^{-1}$ (Jacobson et al., 2007; Resplandy et al., 2018) without considering the uncertainty contribution from this adjustment. We further excluded the air-sea flux estimates provided by Watson et al. (2020) when calculating the ensemble mean and standard deviation of the flux products (see separate analysis below). Analogous to Gruber et al. (2019), the difference between the ocean interior estimates and the surface fluxes of $7.9 \pm 3.8 \text{ Pg C dec}^{-1}$ can plausibly be interpreted as a loss of natural carbon from the ocean to the atmosphere (Table 2). Such natural carbon fluxes are captured by the surface flux products, but are not included in the eMLR(C^*) based estimates of the accumulation of C_{ant} in the ocean's interior (Clement & Gruber, 2018). The 1σ -uncertainty of this residual term is almost half as large as the signal itself, suggesting that while the determined flux is significant, its magnitude is not well constrained. However, postulating a loss of natural carbon for the first decade of our analysis is qualitatively in line with previous studies, which concluded that the stagnation of the ocean carbon sink during the 1990s is due to an anomalously strong outgassing of natural carbon primarily in the Southern Ocean (Landschützer et al., 2015; Le Quééré et al., 2007; Lovenduski et al., 2008). It should be noted that our approach to determine the natural carbon flux as a residual term between the net surface flux and the storage change of anthropogenic carbon is only possible at global scale, because storage changes at regional scales can also occur due to ocean interior transport of anthropogenic carbon.

For the 2004–2014 decade, there is no significant difference between the cumulative surface CO_2 fluxes ($26.5 \pm 1.3 \text{ Pg C dec}^{-1}$) and our ocean interior ΔC_{ant} inventory ($27.3 \pm 2.5 \text{ Pg C dec}^{-1}$), suggesting only a minor global net flux of natural CO_2 across the air-sea interface ($0.9 \pm 2.9 \text{ Pg C dec}^{-1}$). The fact that during the second decade the gain of anthropogenic and the loss of natural carbon weakened simultaneously can plausibly be explained by a weakened ventilation of the ocean interior, induced by changes in circulation and/or stratification (Sallée et al., 2021), which results in lower upward transport rates of natural carbon to the surface and, vice versa, reduced downward transport of C_{ant} into the ocean interior. This coupling was already hypothesized in previous studies that identified a synchronised reduction of both carbon flux components during periods of a weak upper-ocean overturning circulation (DeVries et al., 2017; Lovenduski et al., 2008). Specifically, DeVries et al. (2017) suggested a more vigorous global overturning in the 1990s that drove an increased outgassing of natural CO_2 and uptake of anthropogenic CO_2 , whereas a weaker overturning in the 2000s was found to have the opposite effect. Although the periods of our and their study do not fully overlap, the tendencies toward a weaker anthropogenic carbon uptake agree.

The synchronisation of the uptake of anthropogenic and the outgassing of natural carbon was also observed at a regional scale in the Irminger Sea, where Fröb et al. (2018) detected a sharp increase of the C_{ant} inventory from 2012 to 2015, accompanied by a decline in the natural carbon inventory. This was attributed to a deep convection

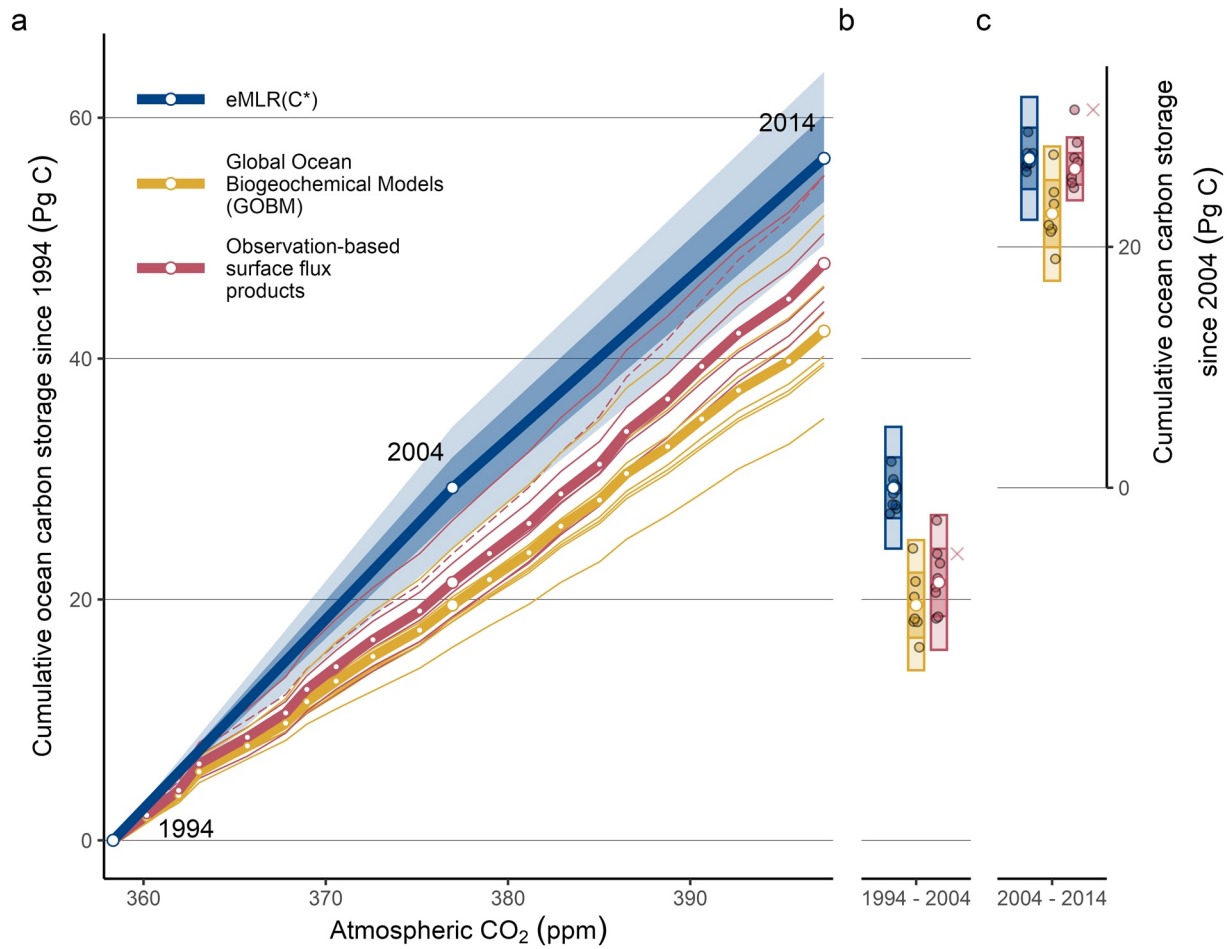


Figure 8. Ocean carbon storage from 1994 to 2014 according to the eMLR(C*) estimates from this study (blue), in comparison to the cumulative fluxes from surface pCO₂ observation-based air-sea CO₂ flux products (red) and Global Ocean Biogeochemical Models (yellow) from the Global Carbon Budget. The ocean carbon storage is displayed in (a) as a function of atmospheric pCO₂ and in (b) and (c) as separate temporal integrals across the two decades of our study. All cumulative estimates for the 2004–2014 period in (c) use the eMLR(C*) estimate for 2004 as the zero point. White points represent the ensemble mean for the GCB estimates and the standard case for the eMLR(C*) estimates. Bars in (b) and (c) indicate 1 σ - and 2 σ -uncertainty ranges. The red dashed line in (a) and red crosses in (b) and (c) represent a CO₂ flux product that is not included in the ensemble and accounts for near-surface temperature gradients (Watson et al., 2020). Note: The eMLR(C*) estimates represent storage changes of anthropogenic carbon only, while the GCB estimates include fluxes of natural and anthropogenic CO₂ (see detailed discussion in the main text).

event during 2015 (Fröb et al., 2016), and underlines that variability at regional scale can superimpose upon the postulated global trend toward a declining anthropogenic carbon uptake.

Our determination of the natural carbon flux as a residual component relies sensitively on the underlying estimates of the net surface CO₂ flux. Watson et al. (2020) recently suggested that the current pCO₂-based flux estimates are all biased low due to their lack of consideration of near-surface temperature gradients. When taking these temperature gradients into consideration, they estimated an ocean carbon sink that is up to 50% larger than the unadjusted estimate. If we used their adjusted flux estimate instead of the ensemble mean of the other flux products as a basis for our calculation of the natural carbon flux (Figure 8), we would determine a release of natural carbon of $5.5 \pm 3.8 \text{ Pg C dec}^{-1}$ for the period 1994–2004 and an uptake of $-4.0 \pm 2.9 \text{ Pg C dec}^{-1}$ for the period 2004–2014. Hence, we would find a weaker loss of natural carbon during the first decade and an uptake of natural carbon rather than a near-zero flux during the second decade. The integral of the natural carbon flux over the two decades would be near zero rather than a net loss. Thus, if we used the temperature adjusted CO₂ flux estimate of Watson et al. (2020), the absolute values of our globally-integrated natural carbon flux estimates would change, but this substitution would not change the conclusion that these fluxes are subject to substantial decadal variability. We note that a recent re-evaluation of the temperature adjustments by Dong et al. (2022) concluded that the effects are likely smaller than suggested by Watson et al. (2020). With the nature and magnitude of these

Table 2

Main Sources and Sinks of CO₂ for the Periods 1994–2004 and 2004–2014 in Pg C dec⁻¹

CO ₂ sources sinks	1994–2004 (Pg C dec ⁻¹)	2004–2014 (Pg C dec ⁻¹)
Total emissions	81.8 ± 7.3	100.3 ± 8.9
Fossil emissions	68.3 ± 3.5	88.2 ± 4.6
Land-use change emissions	13.5 ± 7.9	12 ± 7
Atmospheric sink (Airborne fraction)	39.3 ± 0.2 (48 ± 4%)	44 ± 0.2 (44 ± 4%)
Land sink (Land-borne fraction)	25 ± 4.8 (31 ± 6%)	29.8 ± 5.7 (30 ± 6%)
Ocean sink of C _{ant} (Ocean-borne fraction of C _{ant})	29.3 ± 2.5 (36 ± 4%)	27.3 ± 2.5 (27 ± 4%)
Inferred outgassing of natural carbon	7.9 ± 3.8	0.9 ± 2.9
Net ocean sink (Net ocean-borne fraction)	21.4 ± 2.8 (26 ± 4%)	26.5 ± 1.3 (26 ± 3%)

Note. Estimates of emissions, and the atmospheric, land and net ocean sink are based on the Global Carbon Budget 2021 (Friedlingstein et al., 2022). The net ocean sink estimates represent the cumulative surface fluxes based on surface-pCO₂ observations, adjusted for the outgassing of riverine carbon. The oceanic sink estimates of C_{ant} are from this study, and the oceanic outgassing of natural carbon was determined as the residual between the C_{ant} and the net ocean sink. The uncertainties of the oceanic sink estimates follow the approach of this study, and for all other estimates apply the relative uncertainties for the 2000s according to Table 6 in the GCB (Friedlingstein et al., 2022). Numbers in parentheses indicate the airborne, land-borne, and ocean-borne fractions in % of the total emissions, with propagated uncertainties from the total emissions and the sink terms.

temperature adjustments not yet settled by the community, we stay with the ensemble of unadjusted CO₂ fluxes, but emphasize that the absolute magnitude of the natural CO₂ fluxes inferred from our work may be subject to future revisions. Another need for later revision might arise in the future if recent indications that some ensemble members of the surface flux products overestimate the true decadal variability proved to be correct (Gloege et al., 2021). A final need for revision might arise if our suggested adjustments of the North Pacific data turn out to be erroneous. This would cause no change in the C_{nat} outgassing estimated for the first decade, but it would make the C_{nat} flux larger (more outgassing) during the second decade. In conclusion, there is strong indication that the natural CO₂ flux has been responding sensitively to recent climate change and variability, but the current estimates underpinning the estimation of this component come with too many caveats to provide a hard constraint.

4.3. Implications for the Global Carbon Budget and Climate Change

During the first decade assessed in our study (1994–2004), the flux estimates of the GOBMs (19.5 ± 2.7 Pg C dec⁻¹) and the observation-based flux products (21.4 ± 2.8 Pg C dec⁻¹) are significantly lower than the eMLR(C*)-based estimate (29.3 ± 2.5 Pg C dec⁻¹). In the previous section, we proposed climate-driven outgassing of natural CO₂ from the ocean as a plausible explanation for the discrepancy to the surface flux products. The same argument would apply to the GOBMs, as their flux estimate includes the natural CO₂ flux component. For the 2004–2014 period, the difference between the cumulative observation-based surface fluxes and the ocean interior storage change of C_{ant} disappears, suggesting only a minor global net outgassing of natural CO₂. However, the GOBMs (22.8 ± 2.7 Pg C dec⁻¹, Figure 8) still diagnose a 17% weaker ocean carbon sink during the second decade compared to our ocean interior estimates. The most likely explanation for this discrepancy lies in a combination of three challenges that the majority of the current generation of GOBMs are facing: (a) the surface to deep ocean transport of C_{ant} is rather sluggish, as these ocean models tend to underestimate the ventilation rates of the ocean interior, which was illustrated in structurally similar Earth System Models (Fu et al., 2022; Terhaar et al., 2022), (b) the GOBMs reveal a generally lower decadal variability of the CO₂ fluxes compared to observation-based estimates (Gloege et al., 2021; Hauck et al., 2020), and (c) the non steady-state fluxes of natural CO₂ (i.e., the fluxes that are caused by climate variability) appear to be low in the GOBMs. For example, in the CESM-ETHZ model used in this study, the cumulative flux of natural CO₂ over the 1994–2004 period amounts only to a net uptake of 0.1 Pg C dec⁻¹, and ranges in terms of annual fluxes from an outgassing of 0.2 Pg C yr⁻¹ to an uptake of 0.4 Pg C yr⁻¹, which is substantially lower than the observation-based estimate determined in this study.

Considering these three challenges of the GOBMs, the decadal offsets compared to both observation-based estimates (surface and interior) could be explained as follows: During the first decade, the GOBMs simulate a low anthropogenic CO₂ uptake and a low outgassing of natural CO₂. The compensation of these two biases leads to an

apparent agreement with the surface-flux and ocean interior estimates. For the second decade, the anthropogenic CO₂ uptake in the GOBMs remains low, but this bias is no longer compensated for by the bias in the outgassing of natural CO₂. While this interpretation of the decadal differences between the three groups of estimates is internally consistent, we emphasize that most of the evaluated offsets are of similar magnitude as their uncertainties. A more bottom-up assessment requires the comparison of the different carbon flux components for the ensemble of GOBMs reported in the GCB, an effort that is currently underway in the framework of Phase 2 of the REgional Carbon Cycle Assessment and Processes (RECCAP2) project (Poulter et al., 2022).

To put our ocean carbon sink estimates over the last two decades further into the context of the global carbon cycle, we compare them with the evolution of anthropogenic carbon emissions, as well as with the land and the atmospheric carbon sink extracted from the Global Carbon Budget 2021 (Friedlingstein et al., 2022) for the same periods (Table 2). From this comparison we derive the airborne, ocean-borne and land-borne fraction of the total emissions (Table 2). The ocean-borne fraction of anthropogenic carbon is computed by dividing, for the respective periods, the oceanic sink with the total anthropogenic emissions following the procedures in the GCB (Friedlingstein et al., 2022). In analogy, we report the airborne and land-borne fractions by relating the increase in the atmospheric CO₂ inventory or the land carbon sink to the anthropogenic emissions of CO₂. Note that the global sensitivity β is directly related to these fractions, since it is the ratio between the ocean- and airborne fraction. For the total anthropogenic emissions we consider the emissions due to the combustion of fossil fuels (including the cement carbonation sink) and land use change.

An important aspect for the contextualization of our ocean sink estimates is the increase of the total emissions by about 25% from the first to the second decade of our analysis. In contrast, the growth of the atmospheric sink for CO₂ was only about 10% higher during the second decade, which is reflected in a decrease of the airborne fraction from $48 \pm 4\%$ to $44 \pm 4\%$. Because the emissions grew more rapidly than the atmospheric CO₂, the ocean-borne fraction of C_{ant} (Table 2) decreases even more pronouncedly than the global ocean's uptake sensitivity β (Table 1), namely from $36 \pm 4\%$ to $27 \pm 4\%$ for the 1994–2004 and 2004–2014 decade, respectively, which corresponds to a reduction of the uptake fraction of $-9 \pm 6\%$ (or $\sim 25\%$ in relative terms). In contrast, the land sink evolved very consistently with the total emissions over the two decades, such that the land-borne fraction remained at a stable level ($31 \pm 6\%$ and $30 \pm 6\%$). Due to the identified oceanic outgassing of natural carbon during the first but not the second decade of our analysis, the net ocean sink for anthropogenic and natural carbon increases in a remarkably stable manner with the total emissions. Accordingly, the ocean-borne fraction of the total emissions in terms of the net oceanic CO₂ uptake remained unchanged at a level of $26 \pm 4\%$ and $26 \pm 3\%$. According to our assessment, the sum of all three sink estimates exceeds the total emissions by about 5% during the 1994–2004 period, whereas the sources and sinks of CO₂ during the 2004–2014 period match almost perfectly.

Although we do not identify a change in the net ocean-borne fraction of the total emissions between 1994 and 2014, it is not for granted that the ocean carbon sink will remain constant for the decades to come (Ridge & McKinley, 2021). DeVries et al. (2017) hypothesized that a trend toward a more stratified ocean is likely to strengthen the CO₂ sink in the near future by trapping natural CO₂ in the deep ocean, but further concluded that this process may ultimately limit the net oceanic carbon sink, when the reduced uptake of anthropogenic CO₂ that continues to accumulate in the atmosphere outweighs the reduced outgassing of natural carbon. Our findings demonstrate that these compensating processes are in progress and we deem it of utmost importance to continue the monitoring of the ocean interior accumulation of carbon to keep track of them.

4.4. Caveats and Recommendations

Building on the quantitative uncertainty assessment of our ΔC_{ant} reconstructions (Section 3.4, Text S4 and S5 in Supporting Information S1), we highlight in the following some caveats of our study and provide recommendations on how to overcome them in future studies.

While all sampling periods assigned for this study are relatively well covered with observations, the large changes we reconstruct in the North Atlantic between the first and second period need to be viewed with caution since the number of data records that provide all required variables for the eMLR(C*) analysis is very limited after ~ 2015 . During this period, a reinvigoration of the anthropogenic carbon accumulation has been reported in regional studies (Fröb et al., 2018; Raimondi et al., 2021), albeit only for small subregions of the whole North Atlantic. The inclusion of North Atlantic observations collected since 2015 into an eMLR(C*)-based ΔC_{ant} reconstruction

will contribute to further improve our understanding of the basin-wide C_{ant} storage changes in this highly dynamic region.

We further expect substantially new and improved insights from the completion of another cycle of the repeat hydrography program over the 2020s. In contrast to our two decadal ΔC_{ant} reconstructions, which both build on the same data for the central sampling period (2000s) and are thus not fully independent, reconstructing ocean interior trends with yet another decade of observations would resolve this issue. Furthermore, future investigations based on more recent data will profit from the improved data quality, in particular when becoming independent from the observations of the 1990s, which tend to be less consistent than the more recent measurements (Lauvset et al., 2021).

The continued tracking of the oceanic C_{ant} storage, for example, by providing a global ΔC_{ant} reconstruction for the 2014–2024 period, would also shed light on the very recent divergence of GOBMs and surface-flux products which increased to more than 1 Pg C yr⁻¹ in 2020 (Friedlingstein et al., 2022; Hauck et al., 2020). A burning question in this regard is whether the high uptake determined by the surface flux products around 2020 can be confirmed by ocean interior estimates. Scaling our C_{ant} accumulation estimates from the 2004–2014 period to the 2010s according to the atmospheric CO₂ increase, we would indeed project an uptake of ~32 Pg C dec⁻¹, which is very similar to the mean observation-based net surface flux over the same period.

Another recommendation emerges from the high sensitivity of our results to the adjustments we applied to a subset of the observations provided through GLODAPv2.2021. This pronounced sensitivity highlights the importance of data quality and consistency for the ocean interior observing system. Continued efforts to maintain and improve the quality of seawater biogeochemical measurements, such as through the continued use of reference materials and undertaking inter-laboratory comparisons (Bockmon & Dickson, 2015), are indispensable. Furthermore, the timely submission, compilation, and harmonization of data through GLODAP appears crucial. The release of version 3 of GLODAP including a complete revision of the data adjustments is anticipated in 2024. Based on our findings, we suggest a critical revision of the observation from the Pacific with a particular focus on the TA measurements.

Tightly linked to the observational data consistency is the accuracy of deep ocean ΔC_{ant} reconstructions. Small biases in ΔC_{ant} can indeed exert a strong impact on the basin inventory changes due to the large volume of the deep ocean. Below 1,000 m, the mean ΔC_{ant} reconstructed in this study is lower than 5 $\mu\text{mol kg}^{-1} \text{dec}^{-1}$ across all ocean basins (Figure 4a). Despite the low ΔC_{ant} rates compared to surface waters, the ocean below 1,000 m represents a potentially significant contribution to the global C_{ant} inventory as it accounts for roughly 75% of the total ocean volume. On a global average the content and inventory changes between 1,000 and 3,000 m carry a significant positive signal and contribute about 25% to the total inventory integrated over the top 3,000 m. To derive our global inventories, we have chosen to account for the storage change below 3,000 m (~30% of the total ocean volume) by scaling the inventory with +2% according to the total C_{ant} accumulation at depth in 1994 (Sabine et al., 2004). This approach is consistent with previous studies (Gruber et al., 2019) and represents a compromise between neglecting deep water storage changes and potentially introducing biases from integrating small and highly uncertain ΔC_{ant} below 3,000 m. It is important to note that the general decadal trends reported in this study for the regional inventories are maintained when integrating the reconstructed ΔC_{ant} across the full water column, that is, without the deep ocean scaling (data not shown). Nevertheless, we deem it important that future observation-based studies explicitly include also the accumulation of anthropogenic carbon in the deep ocean below 3,000 m water depth, taking advantage, for example, of measurements of transient tracers, such as SF₆ and CFCs.

Finally, our study revealed that fluxes of natural carbon are key to understanding the oceanic response to a changing climate. The comparison of our estimates of the ocean interior accumulation of anthropogenic carbon with the net surface fluxes of CO₂ allowed us to distinguish a decade with presumably strong net outgassing of natural carbon (1994–2004) from a decade with low net fluxes of natural carbon (2004–2014). However, our quantification of the natural carbon flux as a residual quantity between two entirely independent estimates remains prone to uncertainties that are in the same order of magnitude as the flux itself (McNeil & Matear, 2013). This uncertainty is partly due to remaining uncertainties in the estimates of the surface flux products, some of which might tend to overestimate decadal variability and could be prone to systematic biases such as a missing consideration of near-surface temperature gradients. Furthermore, our testing of the eMLR(C*) method based on synthetic data from a single GOBM with low decadal variability in the anthropogenic carbon storage (see Section 3.4) and low

changes in the natural carbon pool (see Section 4.3) impedes a comprehensive assessment of the method's ability to quantify decadal variability and separate changes in the inventories of natural and anthropogenic carbon. Tests of the method over a larger ensemble of GOBMs, with artificially perturbed data, or time-variant predictor variables may allow further investigation of this aspect. As natural carbon fluxes are expected to vary substantially at sub-decadal time scales, a reoccupation of selected repeat hydrography sections with increased frequency or the extension of the BGC Argo program to global coverage could provide an important observational basis for future studies of ocean interior carbon dynamics. Furthermore, progress in the development of statistical methods to separate storage changes of natural and anthropogenic carbon based on a consistent interpretation of ocean interior observations alone could provide new valuable insight. The application of neural networks to reconstruct ocean interior dynamics of DIC are a meaningful first step in this direction (Broullón et al., 2019, 2020; Keppler et al., 2020, 2023), albeit being based on even fewer data than surface $p\text{CO}_2$ products.

5. Conclusion and Outlook

This study provides the first global reconstruction of the decadal evolution of the ocean interior storage changes of anthropogenic carbon covering the decades 1994 to 2004 and 2004 to 2014. We provide uncertainty estimates for all reported estimates, including regional inventories and spatial distributions of ΔC_{ant} , and decompose the uncertainties into contributions from various configuration choices associated with the eMLR(C*) method.

We find that the oceanic sink for anthropogenic carbon remained strong during both decades ($29 \pm 3 \text{ PgC dec}^{-1}$ and $27 \pm 3 \text{ PgC dec}^{-1}$, respectively). But the sink strength relative to the growth in atmospheric CO_2 (sensitivity β) and the uptake fraction of anthropogenic emissions weakened from the first to the second decade by about 15% and 25%, respectively. We attribute these changes to a decrease of the ocean buffer capacity and a reduction in the surface ocean to deep transport, induced by changes in ocean circulation (most apparent in the Atlantic) and an increase in upper ocean stratification. In contrast to our findings for the accumulation of C_{ant} , observation-based estimates of the surface fluxes of CO_2 indicate that the net ocean sink for anthropogenic and natural carbon increased proportionally with the anthropogenic emissions. This implies that the net ocean uptake fraction remained stable throughout both decades. We attribute the difference between the anthropogenic and the net carbon sink to substantial fluxes of natural carbon that vary between decades, but remain hard to quantify.

Our results can serve as new reference points for the annual ocean sink estimates published in the Global Carbon Budget and provide guidance to further develop and assess GOBMs, which most likely underestimate the anthropogenic carbon sink. Furthermore, our reconstructions of the continuing accumulation of C_{ant} can be used to infer acidification trends in the ocean interior at global scale.

Future studies of the ocean interior storage of C_{ant} may allow us to address questions arising from our analysis, including the drivers for the very recent increase in the net uptake flux as determined based on surface $p\text{CO}_2$ -observations and the question whether compensating processes of the ocean carbon cycle remain effective, such as the regional shift of the anthropogenic carbon storage from the North to the South Atlantic and the apparent coupling between the fluxes of natural and anthropogenic carbon. Mandatory requirements to address these topics are (a) the continued and extended collection of biogeochemical ocean interior observations, that is, the completion of a fourth cycle of the repeat hydrography program and the expansion of the biogeochemical Argo program to global coverage, (b) the continued compilation of the observations into a harmonized and quality-controlled data product, and (c) the continued improvement and further development of statistical methods, for example, to separate the storage changes of anthropogenic and natural carbon.

Conflict of Interest

The authors declare no conflicts of interest relevant to this study.

Data Availability Statement

The anthropogenic carbon estimates reconstructed in this study are available through NCEI's Ocean Carbon and Acidification Data System (OCADS) via the digital object identifier:

<https://doi.org/10.25921/ppcf-w020>.

An identical copy of the data set is also available through the Research Collection of ETH Zurich under the Creative Commons licence Attribution 4.0 International (CC BY 4.0) via the digital object identifier:

<https://doi.org/10.3929/ethz-b-000619627>.

All observational data sets underlying our analysis are publicly available. The merged master file of GLODAPv2.2021 as well as the mapped climatology based on GLODAPv2 were accessed through:

www.glodap.info.

The World Ocean Atlas 2018 climatology data and basin masks were accessed through:

<https://www.ncei.noaa.gov/products/world-ocean-atlas>.

The global gridded data set of the surface ocean carbonate system (OceanSODA-ETHZ) is available under:

<https://doi.org/10.25921/m5wx-ja34>.

The code underlying this study is split up into different processing steps and available through Zenodo under following digital object identifiers.

Preprocessing of observational data: <https://doi.org/10.5281/zenodo.7997243>.

Preprocessing of model data: <https://doi.org/10.5281/zenodo.7997235>.

Running eMLR analysis: <https://doi.org/10.5281/zenodo.4630046>.

Analysing eMLR output: <https://doi.org/10.5281/zenodo.7997221>.

Utility code: <https://doi.org/10.5281/zenodo.7997233>.

Acknowledgments

The authors thank all colleagues that supported and contributed to the collection and harmonisation of high-quality ocean interior observations made available through GLODAP. We are grateful for the formal reviewer comments provided by Andrew Watson and two anonymous reviewers, as well as the informal comments provided on a preprint of this manuscript by Judith Hauck and Jens Terhaar. JDM and NG acknowledge support from the European Union's Horizon 2020 research and innovation programme under grant agreements no. 821003 (project 4C) and no. 821001 (SO-CHIC). FFP was supported by the BOCATS2 (PID2019-104279GB-C21) project funded by MCIN/AEI/10.13039/501100011033 and contributed to WATER:IOS CSIC PTI. AO and SKL were supported by the project N-ICOS-2 (Research Council of Norway Grant 296012). SKL also acknowledges internal funding support from NORCE. MI was supported by JPMEERF21S20810. RW, RAF, and BC were supported by the Office of Ocean and Atmospheric Research (OAR) of NOAA, including the Global Observation and Monitoring Program (GOMO), FundRef 100018302. BC and RAF contributions are PMEL contribution 5454 and CICOES contribution 2022-1244. TT acknowledges support by EU Horizon 2020 through the EuroSea action (grant agreement 862626).

References

- Bittig, H. C., Steinhoff, T., Claustre, H., Fiedler, B., Williams, N. L., Sauzède, R., et al. (2018). An alternative to static climatologies: Robust estimation of open ocean CO₂ variables and nutrient concentrations from T, S, and O₂ data using Bayesian neural networks. *Frontiers in Marine Science*, 5. <https://doi.org/10.3389/fmars.2018.00328>
- Bockmon, E. E., & Dickson, A. G. (2015). An inter-laboratory comparison assessing the quality of seawater carbon dioxide measurements. *Marine Chemistry*, 171, 36–43. <https://doi.org/10.1016/j.marchem.2015.02.002>
- Bopp, L., Lévy, M., Resplandy, L., & Sallée, J. B. (2015). Pathways of anthropogenic carbon subduction in the global ocean. *Geophysical Research Letters*, 42(15), 6416–6423. <https://doi.org/10.1002/2015GL065073>
- Broullón, D., Pérez, F. F., Velo, A., Hoppema, M., Olsen, A., Takahashi, T., et al. (2019). A global monthly climatology of total alkalinity: A neural network approach. *Earth System Science Data*, 11(3), 1109–1127. <https://doi.org/10.5194/essd-11-1109-2019>
- Broullón, D., Pérez, F. F., Velo, A., Hoppema, M., Olsen, A., Takahashi, T., et al. (2020). A global monthly climatology of oceanic total dissolved inorganic carbon: A neural network approach. *Earth System Science Data*, 12(3), 1725–1743. <https://doi.org/10.5194/essd-12-1725-2020>
- Canadell, J. G., Monteiro, P. M. S., Costa, M. H., Cunha, L. C. D., Cox, P. M., Eliseev, A. V., et al. (2021). Global carbon and other biogeochemical cycles and feedbacks. In *IPCC AR6 WGI, final government distribution (p. chapter 5)*. Retrieved from <https://hal.archives-ouvertes.fr/hal-03336145>
- Carter, B. R., Feely, R. A., Wanninkhof, R., Kouketsu, S., Sonnerup, R. E., Pardo, P. C., et al. (2019). Pacific anthropogenic carbon between 1991 and 2017. *Global Biogeochemical Cycles*, 33(5), 2018GB006154. <https://doi.org/10.1029/2018GB006154>
- Cheng, L., Foster, G., Hausfather, Z., Trenberth, K. E., & Abraham, J. (2022). Improved quantification of the rate of Ocean warming. *Journal of Climate*, 35(14), 4827–4840. <https://doi.org/10.1175/JCLI-D-21-0895.1>
- Clement, D., & Gruber, N. (2018). The eMLR(C*) method to determine decadal changes in the global ocean storage of anthropogenic CO₂. *Global Biogeochemical Cycles*, 32(4), 654–679. <https://doi.org/10.1002/2017GB005819>
- Crisp, D., Dolman, H., Tanhua, T., McKinley, G. A., Hauck, J., Bastos, A., et al. (2022). How well do we understand the land-ocean-atmosphere carbon cycle? *Reviews of Geophysics*, 60(2), e2021RG000736. <https://doi.org/10.1029/2021RG000736>
- DeVries, T. (2014). The oceanic anthropogenic CO₂ sink: Storage, air-sea fluxes, and transports over the industrial era. *Global Biogeochemical Cycles*, 28(7), 631–647. <https://doi.org/10.1002/2013GB004739>
- DeVries, T., Holzer, M., & Primeau, F. (2017). Recent increase in oceanic carbon uptake driven by weaker upper-ocean overturning. *Nature*, 542(7640), 215–218. <https://doi.org/10.1038/nature21068>
- DeVries, T., & Primeau, F. (2011). Dynamically and observationally constrained estimates of water-mass distributions and ages in the global ocean. *Journal of Physical Oceanography*, 41(12), 2381–2401. <https://doi.org/10.1175/JPO-D-10-05011.1>
- Dickson, A. G. (1990). Standard potential of the reaction: AgCl(s) + 1/2H₂(g) = Ag(s) + HCl(aq), and the standard acidity constant of the ion HSO₄⁻ in synthetic sea water from 273.15 to 318.15 K. *The Journal of Chemical Thermodynamics*, 22(2), 113–127. [https://doi.org/10.1016/0021-9614\(90\)90074-Z](https://doi.org/10.1016/0021-9614(90)90074-Z)
- Dickson, A. G., & Riley, J. P. (1979). The estimation of acid dissociation constants in seawater media from potentiometric titrations with strong base. I. The ionic product of water—K_w. *Marine Chemistry*, 7(2), 89–99. [https://doi.org/10.1016/0304-4203\(79\)90001-X](https://doi.org/10.1016/0304-4203(79)90001-X)
- Doney, S. C., Lima, I., Feely, R. A., Glover, D. M., Lindsay, K., Mahowald, N., et al. (2009). Mechanisms governing interannual variability in upper-ocean inorganic carbon system and air-sea CO₂ fluxes: Physical climate and atmospheric dust. *Deep Sea Research Part II: Topical Studies in Oceanography*, 56(8), 640–655. <https://doi.org/10.1016/j.dsr2.2008.12.006>
- Dong, Y., Bakker, D. C. E., Bell, T. G., Huang, B., Landschützer, P., Liss, P. S., & Yang, M. (2022). Update on the temperature corrections of global air-sea CO₂ flux estimates. *Global Biogeochemical Cycles*, 36(9), e2022GB007360. <https://doi.org/10.1029/2022GB007360>
- Fay, A. R., Gregor, L., Landschützer, P., McKinley, G. A., Gruber, N., Gehlen, M., et al. (2021). SeaFlux: Harmonization of air-sea CO₂ fluxes from surface pCO₂ data products using a standardized approach. *Earth System Science Data*, 13(10), 4693–4710. <https://doi.org/10.5194/essd-13-4693-2021>
- Fong, M. B., & Dickson, A. G. (2019). Insights from GO-SHIP hydrography data into the thermodynamic consistency of CO₂ system measurements in seawater. *Marine Chemistry*, 211, 52–63. <https://doi.org/10.1016/j.marchem.2019.03.006>
- Friedlingstein, P., Jones, M. W., O'Sullivan, M., Andrew, R. M., Bakker, D. C. E., Hauck, J., et al. (2022). Global carbon budget 2021. *Earth System Science Data*, 14(4), 1917–2005. <https://doi.org/10.5194/essd-14-1917-2022>

- Fröb, F., Olsen, A., Pérez, F. F., García-Ibáñez, M. I., Jeansson, E., Omar, A., & Lauvset, S. K. (2018). Inorganic carbon and water masses in the Irminger Sea since 1991. *Biogeosciences*, *15*(1), 51–72. <https://doi.org/10.5194/bg-15-51-2018>
- Fröb, F., Olsen, A., Våge, K., Moore, G. W. K., Yashayaev, I., Jeansson, E., & Rajasakaren, B. (2016). Irminger Sea deep convection injects oxygen and anthropogenic carbon to the ocean interior. *Nature Communications*, *7*(1), 13244. <https://doi.org/10.1038/ncomms13244>
- Fu, W., Moore, J. K., Primeau, F., Collier, N., Ogunro, O. O., Hoffman, F. M., & Randerson, J. T. (2022). Evaluation of ocean biogeochemistry and carbon cycling in CMIP Earth system models with the international ocean model benchmarking (IOMB) software system. *Journal of Geophysical Research: Oceans*, *127*(10), e2022JC018965. <https://doi.org/10.1029/2022JC018965>
- Gammon, R. H., Cline, J., & Wisegarver, D. (1982). Chlorofluoromethanes in the northeast Pacific Ocean: Measured vertical distributions and application as transient tracers of Upper Ocean mixing. *Journal of Geophysical Research*, *87*(C12), 9441–9454. <https://doi.org/10.1029/JC087iC12p09441>
- Gao, H., Cai, W.-J., Jin, M., Dong, C., & Timmerman, A. H. V. (2022). Ocean ventilation controls the contrasting anthropogenic CO₂ uptake rates between the Western and eastern South Atlantic Ocean basins. *Global Biogeochemical Cycles*, *36*(6), e2021GB007265. <https://doi.org/10.1029/2021GB007265>
- Garcia, H. E., Boyer, T., Baranova, O. K., Locarnini, R., Mishonov, A., Grodsky, A., et al. (2019). In A. Mishonov (Ed.), *World Ocean Atlas 2018: Product documentation*. Retrieved from <https://www.ncei.noaa.gov/products/world-ocean-atlas>
- Gattuso, J.-P., Epitalon, J.-M., Lavigne, H., & Orr, J. (2021). seacarb: Seawater carbonate chemistry. Retrieved from <https://CRAN.R-project.org/package=seacarb>
- Gloege, L., McKinley, G. A., Landschützer, P., Fay, A. R., Frölicher, T. L., Fyfe, J. C., et al. (2021). Quantifying errors in observationally based estimates of ocean carbon sink variability. *Global Biogeochemical Cycles*, *35*(4), e2020GB006788. <https://doi.org/10.1029/2020GB006788>
- Graham, F. S., & McDougall, T. J. (2013). Quantifying the nonconservative production of conservative temperature, potential temperature, and entropy. *Journal of Physical Oceanography*, *43*(5), 838–862. <https://doi.org/10.1175/JPO-D-11-0188.1>
- Gregor, L., & Gruber, N. (2021). OceanSODA-ETHZ: A global gridded data set of the surface ocean carbonate system for seasonal to decadal studies of ocean acidification. *Earth System Science Data*, *13*(2), 777–808. <https://doi.org/10.5194/essd-13-777-2021>
- Gruber, N., Bakker, D. C. E., DeVries, T., Gregor, L., Hauck, J., Landschützer, P., et al. (2023). Trends and variability in the ocean carbon sink. *Nature Reviews Earth & Environment*, *4*(2), 1–16. <https://doi.org/10.1038/s43017-022-00381-x>
- Gruber, N., Clement, D., Carter, B. R., Feely, R. A., van Heuven, S., Hoppema, M., et al. (2019). The oceanic sink for anthropogenic CO₂ from 1994 to 2007. *Science*, *363*(6432), 1193–1199. <https://doi.org/10.1126/science.aau5153>
- Gruber, N., & Sarmiento, J. L. (2002). Large-scale biogeochemical/physical interactions in elemental cycles. In A. R. Robinson, J. J. McCarthy, & B. J. Rothschild (Eds.), *THE SEA: Biological-physical interactions in the oceans* (Vol. 12, pp. 337–399). John Wiley and Sons.
- Gruber, N., Sarmiento, J. L., & Stocker, T. F. (1996). An improved method for detecting anthropogenic CO₂ in the oceans. *Global Biogeochemical Cycles*, *10*(4), 809–837. <https://doi.org/10.1029/96GB01608>
- Hauck, J., Zeising, M., Le Quéré, C., Gruber, N., Bakker, D. C. E., Bopp, L., et al. (2020). Consistency and challenges in the ocean carbon sink estimate for the global carbon budget. *Frontiers in Marine Science*, *7*. <https://doi.org/10.3389/fmars.2020.571720>
- Holliday, N. P., Bersch, M., Berx, B., Chafik, L., Cunningham, S., Florindo-López, C., et al. (2020). Ocean circulation causes the largest freshening event for 120 years in eastern subpolar North Atlantic. *Nature Communications*, *11*(1), 585. <https://doi.org/10.1038/s41467-020-14474-y>
- IPCC. (2019). In H.-O. Pörtner, D. C. Roberts, V. Masson-Delmotte, P. Zhai, M. Tignor, et al. (Eds.), *IPCC special report on the ocean and cryosphere in a changing climate*. Cambridge University Press. <https://doi.org/10.1017/9781009157964>
- Jackett, D. R., & McDougall, T. J. (1997). A neutral density variable for the world's oceans. *Journal of Physical Oceanography*, *27*(2), 27–263. [https://doi.org/10.1175/1520-0485\(1997\)027<0237:andvft>2.0.co;2](https://doi.org/10.1175/1520-0485(1997)027<0237:andvft>2.0.co;2)
- Jackson, L. C., Biastoch, A., Buckley, M. W., Desbruyères, D. G., Frajka-Williams, E., Moat, B., & Robson, J. (2022). The evolution of the North Atlantic Meridional overturning circulation since 1980. *Nature Reviews Earth & Environment*, *3*(4), 1–14. <https://doi.org/10.1038/s43017-022-00263-2>
- Jackson, L. C., Dubois, C., Forget, G., Haines, K., Harrison, M., Iovino, D., et al. (2019). The mean state and variability of the North Atlantic circulation: A perspective from ocean reanalyses. *Journal of Geophysical Research: Oceans*, *124*(12), 9141–9170. <https://doi.org/10.1029/2019JC015210>
- Jacobson, A. R., Fletcher, S. E. M., Gruber, N., Sarmiento, J. L., & Gloor, M. (2007). A joint atmosphere-ocean inversion for surface fluxes of carbon dioxide: 2. Regional results. *Global Biogeochemical Cycles*, *21*(1), GB1019. <https://doi.org/10.1029/2006GB002703>
- Jiang, L.-Q., Carter, B. R., Feely, R. A., Lauvset, S. K., & Olsen, A. (2019). Surface ocean pH and buffer capacity: Past, present and future. *Scientific Reports*, *9*(1), 18624. <https://doi.org/10.1038/s41598-019-55039-4>
- Johnson, K. M., Dickson, A. G., Eiseid, G., Goyet, C., Guenther, P., Key, R. M., et al. (1998). Coulometric total carbon dioxide analysis for marine studies: Assessment of the quality of total inorganic carbon measurements made during the US Indian Ocean CO₂ Survey 1994–1996. *Marine Chemistry*, *63*(1), 21–37. [https://doi.org/10.1016/S0304-4203\(98\)00048-6](https://doi.org/10.1016/S0304-4203(98)00048-6)
- Johnson, K. M., Dickson, A. G., Eiseid, G., Goyet, C., Guenther, P. R., Key, R. M., et al. (2002). Carbon dioxide, hydrographic and chemical data obtained during the nine R/V Knorr cruises comprising the Indian ocean CO₂ survey (WOCE sections I8S19S, I9N, I8N15E, I3, I5W14, I7N, II, I10, and I2, and I2; December 1, 1994–January 22, 1996) [Dataset]. NOAA National Centers for Environmental Information. <https://doi.org/10.3334/CDIAC/OTG.NDP080>
- Keeling, C. D. (1979). The suess effect: 13Carbon-14Carbon interrelations. *Environment International*, *2*(4), 229–300. [https://doi.org/10.1016/0160-4120\(79\)90005-9](https://doi.org/10.1016/0160-4120(79)90005-9)
- Kepler, L., Landschützer, P., Gruber, N., Lauvset, S. K., & Stemmler, I. (2020). Seasonal carbon dynamics in the near-global ocean. *Global Biogeochemical Cycles*, *34*(12), e2020GB006571. <https://doi.org/10.1029/2020GB006571>
- Kepler, L., Landschützer, P., Lauvset, S. K., & Gruber, N. (2023). Recent trends and variability in the oceanic storage of dissolved inorganic carbon. *Global Biogeochemical Cycles*, *37*(5), e2022GB007677. <https://doi.org/10.1029/2022GB007677>
- Key, R. M., Kozyr, A., Sabine, C. L., Lee, K., Wanninkhof, R., Bullister, J. L., et al. (2004). A global ocean carbon climatology: Results from global data analysis project (GLODAP). *Global Biogeochemical Cycles*, *18*(4), GB4031. <https://doi.org/10.1029/2004GB002247>
- Khatiwal, S., Primeau, F., & Hall, T. (2009). Reconstruction of the history of anthropogenic CO₂ concentrations in the ocean. *Nature*, *462*(7271), 346–349. <https://doi.org/10.1038/nature08526>
- Khatiwal, S., Tanhua, T., Mikaloff Fletcher, S., Gerber, M., Doney, S. C., Graven, H. D., et al. (2013). Global ocean storage of anthropogenic carbon. *Biogeosciences*, *10*(4), 2169–2191. <https://doi.org/10.5194/bg-10-2169-2013>
- Lan, X., Tans, P., & Thoning, K. W. (2022). *Trends in globally-averaged CO₂ determined from NOAA global monitoring laboratory measurements. Version 2022-11*. NOAA/GML. Retrieved from gml.noaa.gov/ccgg/trends/
- Landschützer, P., Gruber, N., & Bakker, D. C. E. (2016). Decadal variations and trends of the global ocean carbon sink. *Global Biogeochemical Cycles*, *30*(10), 1396–1417. <https://doi.org/10.1002/2015GB005359>

- Landschützer, P., Gruber, N., Haumann, F. A., Rödenbeck, C., Bakker, D. C. E., van Heuven, S., et al. (2015). The reinvigoration of the Southern Ocean carbon sink. *Science*, *349*(6253), 1221–1224. <https://doi.org/10.1126/science.aab2620>
- Latif, M., Sun, J., Visbeck, M., & Hadi Bordbar, M. (2022). Natural variability has dominated Atlantic meridional overturning circulation since 1900. *Nature Climate Change*, *12*(5), 1–6. <https://doi.org/10.1038/s41558-022-01342-4>
- Lauvset, S. K., Key, R. M., Olsen, A., van Heuven, S., Velo, A., Lin, X., et al. (2016). A new global interior ocean mapped climatology: The 10×10 GLODAP version 2 (p. 16).
- Lauvset, S. K., Lange, N., Tanhua, T., Bittig, H. C., Olsen, A., Kozyr, A., et al. (2021). An updated version of the global interior ocean biogeochemical data product, GLODAPv2.2021. *Earth System Science Data*, *13*(12), 5565–5589. <https://doi.org/10.5194/essd-13-5565-2021>
- Lauvset, S. K., Lange, N., Tanhua, T., Bittig, H. C., Olsen, A., Kozyr, A., et al. (2022). The latest version of the global interior ocean biogeochemical data product. *Earth System Science Data*, *14*(12), 5543–5572. <https://doi.org/10.5194/essd-14-5543-2022>
- Le Quéré, C., Rödenbeck, C., Buitenhuis, E. T., Conway, T. J., Langenfelds, R., Gomez, A., et al. (2007). Saturation of the Southern Ocean CO₂ sink due to recent climate change. *Science*, *316*(5832), 1735–1738. <https://doi.org/10.1126/science.1136188>
- Li, G., Cheng, L., Zhu, J., Trenberth, K. E., Mann, M. E., & Abraham, J. P. (2020). Increasing ocean stratification over the past half-century. *Nature Climate Change*, *10*(12), 1–8. <https://doi.org/10.1038/s41558-020-00918-2>
- Locarnini, R., Mishonov, A., Baranova, O., Boyer, T., Zweng, M., Garcia, H., et al. (2019). World Ocean Atlas 2018, volume 1: Temperature.
- Lovenduski, N. S., Gruber, N., & Doney, S. C. (2008). Toward a mechanistic understanding of the decadal trends in the Southern Ocean carbon sink. *Global Biogeochemical Cycles*, *22*(3), GB3016. <https://doi.org/10.1029/2007GB003139>
- Lueker, T. J., Dickson, A. G., & Keeling, C. D. (2000). Ocean pCO₂ calculated from dissolved inorganic carbon, alkalinity, and equations for K₁ and K₂: Validation based on laboratory measurements of CO₂ in gas and seawater at equilibrium. *Marine Chemistry*, *70*(1), 105–119. [https://doi.org/10.1016/S0304-4203\(00\)00022-0](https://doi.org/10.1016/S0304-4203(00)00022-0)
- McNeil, B. I., & Matear, R. J. (2013). The non-steady state oceanic CO₂ signal: Its importance, magnitude and a novel way to detect it. *Biogeosciences*, *10*(4), 2219–2228. <https://doi.org/10.5194/bg-10-2219-2013>
- McNeil, B. I., Matear, R. J., Key, R. M., Bullister, J. L., & Sarmiento, J. L. (2003). Anthropogenic CO₂ uptake by the ocean based on the global chlorofluorocarbon data set. *Science*, *299*(5604), 235–239. <https://doi.org/10.1126/science.1077429>
- Millero, F. J., Dickson, A. G., Eisele, G., Goyet, C., Guenther, P., Johnson, K. M., et al. (1998). Assessment of the quality of the shipboard measurements of total alkalinity on the WOCE Hydrographic Program Indian Ocean CO₂ survey cruises 1994–1996. *Marine Chemistry*, *63*(1), 9–20. [https://doi.org/10.1016/S0304-4203\(98\)00043-7](https://doi.org/10.1016/S0304-4203(98)00043-7)
- Murata, A., Kumamoto, Y., Sasaki, K., Watanabe, S., & Fukasawa, M. (2010). Decadal increases in anthropogenic CO₂ along 20°S in the South Indian Ocean. *Journal of Geophysical Research*, *115*(C12), C12055. <https://doi.org/10.1029/2010JC006250>
- Olsen, A., Key, R. M., van Heuven, S., Lauvset, S. K., Velo, A., Lin, X., et al. (2016). The global ocean data analysis project version 2 (GLODAPv2)—An internally consistent data product for the World Ocean. *Earth System Science Data*, *8*(2), 297–323. <https://doi.org/10.5194/essd-8-297-2016>
- Olsen, A., Lange, N., Key, R. M., Tanhua, T., Álvarez, M., Becker, S., et al. (2019). GLODAPv2.2019—An update of GLODAPv2. *Earth System Science Data*, *11*(3), 1437–1461. <https://doi.org/10.5194/essd-11-1437-2019>
- Olsen, A., Omar, A. M., Jeansson, E., Anderson, L. G., & Bellerby, R. G. J. (2010). Nordic seas transit time distributions and anthropogenic CO₂. *Journal of Geophysical Research*, *115*(C5), C05005. <https://doi.org/10.1029/2009JC005488>
- Palmieri, J., Orr, J. C., Dutay, J.-C., Béranger, K., Schneider, A., Beuvier, J., & Somot, S. (2015). Simulated anthropogenic CO₂ storage and acidification of the Mediterranean Sea. *Biogeosciences*, *12*(3), 781–802. <https://doi.org/10.5194/bg-12-781-2015>
- Panassa, E., Santana-Casiano, J. M., González-Dávila, M., Hoppema, M., van Heuven, S. M. A. C., Völker, C., et al. (2018). Variability of nutrients and carbon dioxide in the Antarctic Intermediate Water between 1990 and 2014. *Ocean Dynamics*, *68*(3), 295–308. <https://doi.org/10.1007/s10236-018-1131-2>
- Park, G.-H., Lee, K., Tishchenko, P., Min, D.-H., Warner, M. J., Talley, L. D., et al. (2006). Large accumulation of anthropogenic CO₂ in the East (Japan) Sea and its significant impact on carbonate chemistry. *Global Biogeochemical Cycles*, *20*(4), GB4013. <https://doi.org/10.1029/2005GB002676>
- Patara, L., Böning, C. W., & Tanhua, T. (2021). Multidecadal changes in southern ocean ventilation since the 1960s driven by wind and buoyancy forcing. *Journal of Climate*, *34*(4), 1485–1502. <https://doi.org/10.1175/JCLI-D-19-0947.1>
- Perez, F. F., & Fraga, F. (1987). Association constant of fluoride and hydrogen ions in seawater. *Marine Chemistry*, *21*(2), 161–168. [https://doi.org/10.1016/0304-4203\(87\)90036-3](https://doi.org/10.1016/0304-4203(87)90036-3)
- Pérez, F. F., Mercier, H., Vázquez-Rodríguez, M., Lherminier, P., Velo, A., Pardo, P. C., et al. (2013). Atlantic Ocean CO₂ uptake reduced by weakening of the meridional overturning circulation. *Nature Geoscience*, *6*(2), 146–152. <https://doi.org/10.1038/ngeo1680>
- Pérez, F. F., Vázquez-Rodríguez, M., Mercier, H., Velo, A., Lherminier, P., & Ríos, A. F. (2010). Trends of anthropogenic CO₂ storage in North Atlantic water masses. *Biogeosciences*, *7*(5), 1789–1807. <https://doi.org/10.5194/bg-7-1789-2010>
- Poulter, B., Bastos, A., Canadell, J., Ciais, P., Gruber, N., Hauck, J., et al. (2022). Inventorying Earth's land and ocean greenhouse gases. *Eos*, *103*. <https://doi.org/10.1029/2022eo179084>
- Raimondi, L., Tanhua, T., Azetsu-Scott, K., Yashayaev, I., & Wallace, D. W. R. (2021). A 30-year time series of transient tracer-based estimates of anthropogenic carbon in the central Labrador Sea. *Journal of Geophysical Research: Oceans*, *126*(5), e2020JC017092. <https://doi.org/10.1029/2020JC017092>
- Resplandy, L., Keeling, R. F., Rödenbeck, C., Stephens, B. B., Khatiwala, S., Rodgers, K. B., et al. (2018). Revision of global carbon fluxes based on a reassessment of oceanic and riverine carbon transport. *Nature Geoscience*, *11*(7), 504–509. <https://doi.org/10.1038/s41561-018-0151-3>
- Ridge, S. M., & McKinley, G. A. (2021). Ocean carbon uptake under aggressive emission mitigation. *Biogeosciences*, *18*(8), 2711–2725. <https://doi.org/10.5194/bg-18-2711-2021>
- Ríos, A. F., Velo, A., Pardo, P. C., Hoppema, M., & Pérez, F. F. (2012). An update of anthropogenic CO₂ storage rates in the Western South Atlantic basin and the role of Antarctic Bottom Water. *Journal of Marine Systems*, *94*, 197–203. <https://doi.org/10.1016/j.jmarsys.2011.11.023>
- Sabine, C. L., Feely, R. A., Gruber, N., Key, R. M., Lee, K., Bullister, J. L., et al. (2004). The oceanic sink for anthropogenic CO₂. *Science*, *305*(5682), 367–371. <https://doi.org/10.1126/science.1097403>
- Sabine, C. L., Key, R. M., Johnson, K. M., Millero, F. J., Poisson, A., Sarmiento, J. L., et al. (1999). Anthropogenic CO₂ inventory of the Indian Ocean. *Global Biogeochemical Cycles*, *13*(1), 179–198. <https://doi.org/10.1029/1998GB900022>
- Sallée, J.-B., Pellichero, V., Akhondas, C., Pauthenet, E., Vignes, L., Schmidtke, S., et al. (2021). Summertime increases in upper-ocean stratification and mixed-layer depth. *Nature*, *591*(7851), 592–598. <https://doi.org/10.1038/s41586-021-03303-x>
- Sarmiento, J. L., & Gruber, N. (2006). *Ocean biogeochemical dynamics*. Princeton University Press.
- Sharp, J. D., & Byrne, R. H. (2020). Interpreting measurements of total alkalinity in marine and estuarine waters in the presence of proton-binding organic matter. *Deep Sea Research Part 1: Oceanographic Research Papers*, *165*, 103338. <https://doi.org/10.1016/j.dsr.2020.103338>

- Shi, J.-R., Talley, L. D., Xie, S.-P., Peng, Q., & Liu, W. (2021). Ocean warming and accelerating Southern Ocean zonal flow. *Nature Climate Change*, *11*(12), 1–8. <https://doi.org/10.1038/s41558-021-01212-5>
- Sloyan, B. M., Wanninkhof, R., Kramp, M., Johnson, G. C., Talley, L. D., Tanhua, T., et al. (2019). The global ocean ship-based hydrographic investigations program (GO-SHIP): A platform for integrated multidisciplinary ocean science. *Frontiers in Marine Science*, *6*. <https://doi.org/10.3389/fmars.2019.00445>
- Talley, L. d., Feely, R. a., Sloyan, B. m., Wanninkhof, R., Baringer, M. o., Bullister, J. l., et al. (2016). Changes in ocean heat, carbon content, and ventilation: A review of the first decade of GO-SHIP global repeat hydrography. *Annual Review of Marine Science*, *8*(1), 185–215. <https://doi.org/10.1146/annurev-marine-052915-100829>
- Tanhua, T., Jones, E. P., Jeansson, E., Jutterström, S., Smethie, W. M., Wallace, D. W. R., & Anderson, L. G. (2009). Ventilation of the Arctic Ocean: Mean ages and inventories of anthropogenic CO₂ and CFC-11. *Journal of Geophysical Research*, *114*(C1), C01002. <https://doi.org/10.1029/2008JC004868>
- Terhaar, J., Frölicher, T. L., & Joos, F. (2022). Observation-constrained estimates of the global ocean carbon sink from Earth system models. *Biogeosciences*, *19*(18), 4431–4457. <https://doi.org/10.5194/bg-19-4431-2022>
- Tsujino, H., Urakawa, S., Nakano, H., Small, R. J., Kim, W. M., Yeager, S. G., et al. (2018). JRA-55 based surface dataset for driving ocean–sea-ice models (JRA55-do). *Ocean Modelling*, *130*, 79–139. <https://doi.org/10.1016/j.ocemod.2018.07.002>
- Wallace, D. W. R. (1995). Monitoring global ocean carbon inventories.
- Wanninkhof, R., Doney, S. C., Bullister, J. L., Levine, N. M., Warner, M., & Gruber, N. (2010). Detecting anthropogenic CO₂ changes in the interior Atlantic Ocean between 1989 and 2005. *Journal of Geophysical Research*, *115*(C11), C11028. <https://doi.org/10.1029/2010JC006251>
- Watson, A. J., Schuster, U., Shutler, J. D., Holding, T., Ashton, I. G. C., Landschützer, P., et al. (2020). Revised estimates of ocean-atmosphere CO₂ flux are consistent with ocean carbon inventory. *Nature Communications*, *11*(1), 4422. <https://doi.org/10.1038/s41467-020-18203-3>
- Weiss, R. F. (1970). The solubility of nitrogen, oxygen and argon in water and seawater. *Deep Sea Research and Oceanographic Abstracts*, *17*(4), 721–735. [https://doi.org/10.1016/0011-7471\(70\)90037-9](https://doi.org/10.1016/0011-7471(70)90037-9)
- Woosley, R. J., Millero, F. J., & Wanninkhof, R. (2016). Rapid anthropogenic changes in CO₂ and pH in the Atlantic Ocean: 2003–2014. *Global Biogeochemical Cycles*, *30*(1), 70–90. <https://doi.org/10.1002/2015GB005248>
- Yang, S., Gruber, N., Long, M. C., & Vogt, M. (2017). ENSO-driven variability of denitrification and suboxia in the eastern Tropical Pacific Ocean. *Global Biogeochemical Cycles*, *31*(10), 1470–1487. <https://doi.org/10.1002/2016GB005596>
- Young, I. R., & Ribal, A. (2019). Multiplatform evaluation of global trends in wind speed and wave height. *Science*, *364*(6440), 548–552. <https://doi.org/10.1126/science.aav9527>
- Zweng, M. M., Reagan, J., Seidov, D., Boyer, T., Locarnini, R., Garcia, H., et al. (2019). *World Ocean Atlas 2018 volume 2*. Salinity.

Erratum

In the originally published version of this article, the sole line equation in Section S4.1 in the supporting information did not render correctly. The error has been corrected, and this may be considered the authoritative version of record.